The Upper Atmosphere of Uranus from Stellar Occultations I: Methods and Validation

William R. Saunders,[1,2] Michael J. Person,[3] Paul Withers,[1,4] Richard G. French,[5] and Chanita Tubthong[6]

[1]*Department of Astronomy, Boston University, Boston, MA 02215, USA*
[2]*NASA FINESST Fellow*
[3]*Department of Earth, Atmospheric, and Planetary Sciences, Massachusetts Institute of Technology (MIT), Cambridge, MA 02139-4307, USA.*
[4]*Center for Space Physics, Boston University, Boston, MA 02215, USA*
[5]*Department of Astronomy, Wellesley College, Wellesley, MA 02481, USA*
[6]*Department of Physics and Astronomy, Tufts University, Medford, MA 02155, USA*

ABSTRACT

Measurements made by the Voyager 2 spacecraft during its flybys of Uranus in 1986 found warm stratospheric and hot thermospheric temperatures that cannot be explained by solar energy alone. It contributes to what has become known as the "giant planet energy crisis"; there is a fundamental lack of understanding of the energy balance of giant planets in the Solar System. Uranus, in particular, has both the hottest thermospheric temperatures and the weakest internal heat flux of all four giant planets. Moreover, the Voyager 2 UV temperature measurements are at odds with the many contemporaneous Earth-based stellar occultation observations. In this work, we examine the 1977 Uranus stellar occultation (U0) and compare the observed light curve to reported Voyager 2 temperature profiles by simulating the latter into stellar occultation light curves. In this investigation we find that the observed light curves are in tension with the simulated light curves to a high degree of statistical confidence. Next, we reprocess the U0 light curves using a modern approach, with some significant adjustments described herein, and report updated profiles. We find that the lower thermosphere of Uranus is much cooler than the Voyager 2 profiles suggest, but slightly warmer than those originally-published from the U0 occultation. In Paper II, we will present the results of applying these methods to many of the dozens of archival Uranus stellar occultations.

1. INTRODUCTION

The thermal structure of a planetary atmosphere provides important insights into the total energy balance of a planet, meridional, latitudinal, and vertical mixing, chemical and photochemical reactions, condensation and precipitation, radiative transfer, and atmospheric waves (see Catling 2015, for a comprehensive review). The thermal structure of the atmosphere of Uranus is of particular importance. In addition to those general aspects highlighted above, Uranus has an extremely unusual obliquity of 98 degrees, which leads to unique seasonal and meridional patterns in atmospheric processes and properties. Moreover, Uranus has much higher upper atmospheric temperatures than can be explained by solar heating alone (Marley & McKay 1999; Melin 2020a; Fletcher et al. 2020) (a striking example of the "giant planet energy crisis"), yet has a much weaker internal energy source than the other giant planets (Pearl et al. 1990; Bishop et al. 1995). Uranus is also an accessible representative of one of the most abundant types of exoplanets – ice giants (Borucki et al. 2010; Winn & Fabrycky 2015; Sumi et al. 2016; Fulton & Petigura 2018). Finally, Uranus

Corresponding author: William R. Saunders
wsaund@bu.edu

was recommended as the target of NASA's next major flagship mission by the 2023-2032 Planetary Science Decadal Survey (NASEM 2022).

The upper atmospheres of Jupiter, Saturn, and Neptune are also much hotter than can be explained by solar and internal heating (Mueller-Wodarg et al. 2008), yet recent work has suggested a solution to this heating problem at Jupiter and Saturn that combines wave activity and auroral heating (Koskinen et al. 2015; Melin 2020b; O'Donoghue et al. 2021). The thermal structure of the atmosphere of Uranus, by contrast to Jupiter and Saturn, is poorly constrained by observations, making it difficult to test such theories.

Figure 1 compares vertical temperature-pressure profiles of Uranus observed by the Voyager 2 spacecraft with those made from ground-based observations. To date, the only spacecraft encounter with Uranus was the flyby of Voyager 2 in 1986. Radio occultation observations by Voyager 2 yielded two temperature profiles (ingress and egress) that span from 2200 mbar to 0.25 mbar (Lindal et al. 1987). While these profiles probed significantly different planetary longitudes and local solar times, the geometry of Uranus near southern hemisphere solstice meant that the ingress and egress had approximately the same latitude. These two profiles agree to within a few K, as can be seen on Figure 1.

Ultraviolet stellar and solar occultation observations by Voyager 2 yielded several temperature profiles that span from 0.05 mbar to 1×10^{-8} mbar (Herbert et al. 1987, hereafter H87). As discussed in Section 2, these observations were challenging to process and interpret. The original analysis by the Voyager 2 experimenters reported a solar occultation temperature profile (ingress only) that consisted of four temperature values spanning 5–6 orders of magnitude in pressure. They also reported a stellar occultation temperature profile with similar characteristics that was based on observations of both the ingress and the egress of the star γ Pegasi. An alternative representation of the Voyager 2 UV temperature profiles has also been widely used. A simple numerical model was constructed based upon the thermal conductivity equation and fit to the H87 results (Stevens et al. 1993, hereafter S93). H87 reported two profiles: the stellar occultation (combining ingress and egress) and the solar occultation ingress. S93 published three modeled temperature profiles: the stellar occultation ingress, the stellar occultation egress, and the solar occultation ingress.

Ground-based stellar occultation observations of Uranus at visible and near-infrared wavelengths have been acquired for dozens of opportunities since 1977. They typically span from 0.1 mbar to 5×10^{-4} mbar. Figure 1 shows only the "U0" occultation from March 1977 (Elliot & Dunham 1979). Temperature profiles from subsequent ground-based stellar occultations are broadly similar (see, e.g., French et al. 1982; Sicardy et al. 1982; French et al. 1983; Sicardy et al. 1985; French et al. 1987; Millis et al. 1987; Elliot et al. 1987; Young et al. 2001).

These three remote-sensing measurements of Uranus—Voyager radio occultations, Voyager stellar occultations, and Earth-based stellar occultations—are the only independent measurements of the vertical temperature structure of Uranus. Thermal infrared measurements made by Spitzer and forthcoming JWST measurements do produce vertical temperature profiles in the lower atmosphere, but require a prior, for which the H87 profiles are typically used (Orton et al. 2014; Rowe-Gurney et al. 2021). Therefore, these are not truly independent measurements.

Figure 1 shows large differences in temperature at the 1 μbar level between the U0 Earth-based stellar occultation (two instances, circa 100 K) and the Voyager 2 UV occultations (three instances, circa 300 K). The Earth-based stellar occultation and the Voyager 2 UV solar (but not stellar) occultation essentially make measurements around the day-night terminator, so both types of observations reflect sunrise/sunset conditions. Additionally, because the Earth-based stellar occultation and UV solar occultation were both observed near Uranus southern hemisphere solstice and Uranus has a 98° obliquity, both probe the equatorial region. Uncertainties were reported for the ground-based stellar occultation temperature profiles, but not for the Voyager 2 UV occultations.

Two fundamental questions motivate the aims of this work. Question 1: Are Earth-based stellar occultation temperature profiles consistent with Voyager 2 UV temperature profiles? As mentioned above and shown in Figure 1, there are hundreds-of-Kelvin discrepancies between the upper portion of the U0 profile and the Voyager 2 profiles at the same pressure level. Question 2: What is the upper atmospheric structure of Uranus? To answer these questions, we develop and apply two independent methods to dozens of archival Earth-based stellar occultation observations made between 1977 and 1998. In Paper I, we focus on the development of these two methods and demonstrate them using a high-quality test case: the U0 occultation from March 1977. In Paper II (in preparation), we will present the results of applying these methods to the many archival Earth-based occultations.

The two methods used in this paper are "forward modeling" and "inversion with model fitting." First, forward modeling is the procedure by which we synthesize the fundamental observable, the time series of stellar brightness, that would be seen if a ground-based stellar occultation sampled the Uranian atmospheric conditions reported from the

Voyager 2 UV occultations (Chamberlain & Elliot 1997, hereafter CE97). We examine whether or not this synthetic light curve is consistent with the actual light curve seen in the U0 Earth-based stellar occultation. Second, to process a stellar occultation, we use an improved version of the model fitting and inversion steps used to generate temperature profiles from the U0 occultation (Elliot & Young 1992; Elliot et al. 2003). There are several improvements to the original processing method from 1977: we use the full-resolution data, we use a more realistic boundary condition, and we are no longer subject to the bias caused by the previous method of handling negative flux measurements. Full details on these improvements are provided in Section 4. We compare the improved U0 temperature profile to the Voyager 2 UV temperature profiles as well as the original analysis (Elliot et al. 1977b).

The structure of this article is as follows. In Section 2, we provide further details on the historic, remote-sensing measurements of the atmosphere of Uranus. In Section 3, we describe the forward modeling procedure to simulate an Earth-based stellar occultation light curve for a chosen Uranian atmospheric profile. In Section 4, we describe the updated processing procedure to create temperature profiles from an occultation light curve. In Sections 5 and 6 we show the results of applying these two methods to the U0 occultation. In Section 7, we discuss and interpret our preliminary findings from applying these methods to the U0 validation case. In Section 8, we offer preliminary conclusions and discuss how we will apply the methods presented herein to the many additional stellar occultations that will comprise the scope of Paper II.

2. URANUS REMOTE SENSING MEASUREMENT DETAILS

As explained in Section 1, there have been three truly independent methods of remote-sensing the vertical temperature structure of Uranus. (1) Voyager 2 radio occultations; (2) Voyager 2 UV stellar and solar occultations; (3) Earth-based stellar occultations.

The first two methods were both conducted by Voyager 2 during its flyby of Uranus in 1986. The radio occultation experiment, using the Radio Science System (Eshleman et al. 1977), observed the refraction and frequency shift (by the lower atmosphere) of a transmitted radio signal, which was used to infer atmospheric properties (Lindal et al. 1987). These measurements produced temperature profiles extending from the troposphere to the lower stratosphere (pressure between 2200 and 0.25 mbar). Since the flyby occurred during southern hemisphere summer and Uranus has a $98°$ obliquity, the radio occultation experiment probed the lower atmosphere in the equatorial region of the planet. Uranus was found to have a cold troposphere ($T_{tropopause} = 53 \pm 1$ K at 100 mbar) and a gradually-warming stratosphere ($T_{stratopause} = 114 \pm 10$ K at 0.5 mbar) (Lindal et al. 1987). A methane cloud base was detected at about 1.2 bar, with the atmosphere above determined to be clear. Detailed analysis of the Raman scattered Lyman-α emissions using the Voyager 2 Ultraviolet Spectrometer (UVS) found the atmosphere about 0.5 mbar to be devoid of hydrocarbons (Yelle et al. 1987).

Voyager stellar and solar UV occultations were observed using the UVS instrument (Broadfoot et al. 1977), which had 126 spectral channels of width 0.926 nm each, spanning the wavelength range 53–170 nm in the ultraviolet. Two occultations were observed: a solar occultation (ingress only) and a stellar occultation of γ Pegasi (ingress and egress). A comprehensive description of how these observations were acquired and processed is given by H87.

During a spacecraft UV occultation, observed time-series spectra measure extinction (mostly absorption) by atmospheric species. Using the known cross-sectional area of each species as a function of wavelength, it is possible to infer the density of the atmosphere at various radii, and then determine a temperature and pressure by using hydrostatic equilibrium and the ideal gas law. In the H87 processing of the UV occultations, there are four measurements of temperature at different altitudes, each made by using one spectral feature. (See Figure 4 in H87 for a visual summary of the altitudes probed by these bands).

(1) The H_2 continuum absorption ($\sim$53–70 nm) probed the highest region of the atmosphere, at pressure levels of about $2\times10^{-8} - 5\times10^{-9}$ mbar (altitude of about $4500 - 5500$ km above the 1 bar pressure level). The cross section of the H_2 continuum absorption was well-known at the time, rendering these spectral features among the most reliable. (2) Atomic H continuum absorption ($\sim$70–91 nm) probed the pressure levels of about $1 \times10^{-5} - 1\times10^{-7}$ (altitude of about $2000 - 4000$ km). (3) H_2 Lyman and Werner bands ($\sim$91–110 nm) probed the region of about $5 \times10^{-4} - 1\times10^{-6}$ mbar (altitudes of about $1000 - 2500$ km). These bands, however, posed a major challenge for analysis. "H_2 band absorption actually consists of a great many unresolved lines of highly variable cross section whose average behavior very approximately mimics a continuous absorption with cross section intermediate between the H_2 continuum and H_2 Rayleigh scattering" (H87). As this quote implies, the H_2 bands were the least reliable atmospheric measurements produced from these observations. (4) H_2 Rayleigh scattering ($\sim$159–163 nm) was detectable at Uranus due to the

relatively clear upper atmosphere and probed pressure levels of about $0.81 - 0.02$ mbar (altitude of about $200 - 400$ km). This cross-section is well-known.

From each individual absorption feature, H87 produced values of density, temperature, and pressure at a representative altitude. This comprises four $T(p(r))$ points in the upper atmosphere of Uranus, with an extensive vertical scale but limited vertical resolution (4 points over a vertical distance of $\sim$5000 km). H87 connected these points into a continuous profile using a thermal gradient defined by $T = T_0(p/p_0)^\alpha$, where the values of each measurement and α are given in Table 1 of H87 and the connected profiles are shown in Figure 1 with an additional anchor point from the radio occultation profile and an isothermal extension into the exosphere.

Further analysis of the Voyager 2 stellar and solar UV occultations, as well as the H87 profiles, was conducted by Stevens et al. (1993, hereafter S93). S93 designed a smooth thermospheric model including heat sources in the upper atmosphere conducting downward and a potential heat sink in the lower thermosphere. The number of sources and sinks, as well as the parameters of each, were determined by a least squares fit to the H87 profiles. S93 produced a model for each occultation profile (stellar ingress, stellar egress, and solar ingress). The best fit versions of these models are given in Table III of S93 and include only a single heat source in the upper atmosphere with an approximate flux of 0.06 erg cm^{-2}s^{-1} (6×10^{-5} Wm^{-2}). As noted by the authors, this flux cannot be accounted for by solar irradiance alone. These three models are shown as dotted lines in Figure 1.

In 1977, the first Earth-based stellar occultation by Uranus (given the designation U0) was observed (Elliot & Dunham 1979; Dunham et al. 1980). This observation was monumental in that it enabled the discovery of the rings of Uranus (Elliot et al. 1977a). The observation also made the first vertical temperature measurements of the middle-to-upper atmosphere of Uranus ($\sim$0.1μbar–100μbar). Figure 2 shows the geometry of the occultation, where the black line is the projected chord of the star on the disk of Uranus, moving from green to red. During an Earth-based stellar occultation, light from a distant star is refracted by passing through the occulting atmosphere, refraction that varies as a function of the distance of each ray of light to the center of the planet. The observed stellar flux is used to infer the properties of the occulting planet's atmosphere at various altitude levels, with high vertical resolution. Sections 3 and 4 explain the physics of a stellar occultation in greater detail.

The U0 occultation star was SAO 158687 (V band magnitude of 8.8) and the occultation occurred at approximately 21:00 UTC on March 10, 1977. The event was first predicted in 1973 (Taylor 1973) and details about the observing plan were published in the month before the occultation (Elliot et al. 1977c). Observations were made by a coordinated group of ground-based observers as well as aboard the Kuiper Airborne Observatory (KAO), however, only the Cape Town and KAO observations recorded the atmospheric occultation (others recorded only ring occultations). The data from the KAO (in three channels) are the highest resolution and the only data that survive to the present day. Table 1 shows the basic properties of this observation and the retrieved light curve. In defining the "quality" of a stellar occultation, we often report the signal-to-noise per scale height $(S/N)_H$ as defined in Equation 1 from Elliot et al. (2003):

$$(S/N)_H = \frac{S/N}{\sqrt{\Delta y/H}}, \tag{1}$$

where y is the projected distance of the occulted star from the center of the planetary disk, Δy is the change in this quantity between integration steps, and H is the atmospheric scale height of Uranus. Signal-to-noise per scale height is a useful quantity because it is independent of integration time. Signal-to-noise increases by the square-root of the integration time, and Δy increase linearly with the integration time, so signal-to-noise per scale height does not change. The inclusion of scale height keeps the quantity unitless.

Figure 1 compares the temperature-pressure profiles produced by these three remote-sensing measurements: Voyager 2 radio occultations, Voyager 2 UV stellar and solar occultations, and the U0 Earth-based stellar occultation. From Figure 1, we can see a clear discrepancy between the temperatures retrieved from the U0 occultation and the temperatures produced by the H87 analysis and S93 models. The lower end of the H87 points ($\sim$100–150 K and 0.1–0.2 mbar) are close to the lower end of the U0 temperature profile. Moving upward to the next H87 points at 10^{-3} mbar, we see a strong discrepancy between the UV stellar occultation in green at 200 K and the UV solar occultation in red at 475 K. Though no uncertainties were published for the Voyager 2 UV occultation profiles, the difference between these two temperatures at the same pressure level gives a possible indication of the scale of uncertainties. The next higher UV stellar measurement is at $\sim 2 \times 10^{-4}$ mbar and 500 K. Compared with the 80–100 K U0 measurements, the 200 K Voyager 2 measurement is much warmer and the 475–500 K measurements are significantly hotter. It's important

to note here that the H87 points at $\sim 10^{-3}$–10^{-4} mbar and $\sim$500 K were retrieved from the H_2 Lyman and Werner bands, which, as mentioned above, were unresolved by Voyager 2 and hence the least reliable.

Comparing the S93 models in dotted lines on Figure 1 to the U0 profiles, we see that there is no region of close agreement, even at the lower end of the U0 profiles. Considering that the S93 models are smooth and fit to all H87 points, this is unsurprising.

The Voyager 2 UVS data at Uranus has not been reanalyzed but the Voyagers 1 and 2 UVS data at Saturn has been reanalyzed (Smith et al. 1983; Vervack & Moses 2015). Figure 12 in Vervack & Moses (2015) shows reprocessed temperatures for the six profiles from Voyagers 1 and 2, which have variations in temperature between about 150 and 300 K at 10^{-4} mbar, indicating this region is uncertain for Saturn as well as for Uranus.

We note that the Voyager 2 flyby occurred in 1986 whereas the U0 occultation occurred in 1977. Observations of the H_3^+ ion, which probe temperatures above the homopause (pressure levels of roughly 10^{-4} to 10^{-8} mbar (Moore et al. 2019)), have found a roughly 8 K / year decreasing thermospheric temperature since the early 1990s (Trafton et al. 1993; Melin et al. 2019; Melin 2020a). Though it's possible seasonal variations at Uranus may account for *some* of the temperature differences between U0 and Voyager 2 UVS observations ($\sim$70 K according to H_3^+), the degree of discrepancy shown in Figure 1 cannot be explained by these variations alone. Furthermore, these differences cannot be explained by latitude variations alone either. The U0 occultation probed equatorial regions (see Table 1), similar to the UVS solar occultation, whereas the UVS stellar occultation probed regions of high latitude ($\sim\pm64°$). And yet, Figure 1 shows the greater tension between the U0 profile and the UVS *solar* occultation.

3. FORWARD MODELING PROCEDURE

As discussed in Section 1, there are two procedures of primary focus in this work: forward modeling and inversion with model fitting. The latter takes a time series of stellar brightness that changes as the star is occulted by the planet of interest (an Earth-based stellar occultation "light curve") and produces an atmospheric profile (temperature, pressure, and number density versus altitude). In Section 4, we explain the steps of this method in detail. Forward modeling, by contrast, takes an atmospheric profile and produces a simulated Earth-based stellar occultation light curve. Importantly, forward modeling does not modify the observations; it enables a comparison between an observed light curve and an atmospheric profile. This is why we choose to present forward modeling first in this work—we seek to determine whether or not the atmospheric profiles of Uranus created from Voyager 2 observations are consistent with Earth-based observations of Uranus stellar occultations. Forward modeling enables this comparison without the limitations of model fitting and inversion, which we discuss in Section 4.

3.1. *Overview of Theory*

We use the forward modeling procedure developed by CE97. We first provide an overview of the theory behind this procedure and discuss its implementation. For exhaustive detail, the reader is directed to CE97.

Figure 3 illustrates the geometry of a stellar occultation, during which rays of light emitted sequentially by a distant star pass closer and closer to the center of an occulting planet. The effect of the atmosphere is to bend a given light ray by an amount θ. The close approach distance of a refracted light ray to the planet is given by r. The projected position of the observer relative to the center of the disk of the planet is given by y. Another way to think about it is that y would be the close approach distance of an *unrefracted* light ray. During a stellar occultation, y decreases until it reaches some minimum, which we call the "impact parameter", before increasing symmetrically. D is the distance from the planet to the observer.

A pair of sequential light rays are separated by a distance dr at the planet but are received at Earth separated by a distance dy. As Figure 3 illustrates, $dy \geq dr$, so the received stellar flux decreases as the occultation proceeds by a factor dy/dr. This approximation assumes the occulting atmosphere is cylindrical in the plane defined by the relative motion of the occulting planet with respect to Earth. We next add in the spherical nature of the occulting atmosphere, which has the effect of slightly focusing the rays by a factor of y/r. For a nice illustration of this effect, the reader is referred to Figure 7 in Sicardy (2022). Last, we allow received flux to be extinguished along the ray path, given by $\exp\left[-\tau_{obs}(r)\right]$.

Combining these three effects, we find that the normalized flux ϕ during a stellar occultation can be written

$$\phi = \left|\frac{1}{dr/dy}\right|\left|\frac{1}{y/r}\right|e^{-\tau_{obs}(r)}. \tag{2}$$

In the case of the giant planets, the extinction term is negligible because the atmospheres are clear in the pressure

ranges probed by this technique ($\sim 0.1 - 100\mu$bar) (Yelle et al. 1987). By noticing that

$$y = r + D\theta(r), \tag{3}$$

where we have taken the small-angle approximation $\tan(\theta) \approx \theta$, we can rewrite Equation 2 as

$$\phi = \left| \frac{1}{1 - D\frac{d\theta}{dr}} \right| \left| \frac{1}{1 - D\frac{\theta}{r}} \right|. \tag{4}$$

Using Equation 4 and the relationship between r and y, it is possible to calculate flux ϕ given bending angle θ and observer position y.

From Fermat's principle, the following relation can be derived between the bending angle θ and refractive index N (See Section 3.2 of Born & Wolf (2013) and/or Section 3.2 of Sicardy (2022)):

$$\theta(r) = \int_{-\infty}^{\infty} \frac{r}{r'} \frac{d}{dr'} \ln N(r') dx, \tag{5}$$

where $x^2 = r'^2 - r^2$, as shown in Figure 3 and N is index of refraction. Following CE97, we substitute refractivity $\nu = N - 1$ for index of refraction and make the approximations that $\nu \ll 1$ and $\theta \ll 1$, which allows us to use a first-order Taylor approximation to write Equation 5 as

$$\theta(r) = \int_{-\infty}^{\infty} \frac{r}{r'} \frac{d\nu(r')}{dr'} dx. \tag{6}$$

Equation 6 and its first derivative with respect to r can be used to solve Equation 4 for ϕ.

We find the refractivity ν by relating it to number density n by the equation

$$n(r) = L \frac{\nu(r)}{\nu_{STP}(r)}, \tag{7}$$

where L is Loschmidt's number and $\nu_{STP}(r)$ is the refractivity of the atmosphere at standard temperature and pressure. Most stellar occultation analyses (CE97); (Elliot et al. 2003) assume a homogeneous atmosphere but here we allow composition to vary with altitude, which will be discussed more in Section 5. We find number density by solving the hydrostatic equation

$$\frac{dp}{dr} = -m_{\mathrm{amu}}\mu(r)n(r)g(r), \tag{8}$$

where m_{amu} is the atomic mass unit, μ is the mean molecular weight of the atmosphere, and g is the gravitational acceleration, along with the ideal gas law

$$p = nk_BT, \tag{9}$$

where k_B is Boltzmann's constant.

Equations 8 and 9 can be solved for all variables given mean molecular weight $\mu(r)$, a reference radius r_0, a reference pressure p_0, and either a temperature-pressure or temperature-radius profile. If given a temperature-pressure profile, we can solve for radius by writing Equations 8 and 9 as

$$\mu \int_{r_0}^{r} m(r')g(r')dr' = -\int_{p_0}^{p} \frac{1}{p'} k_BT dp'. \tag{10}$$

If given a temperature-radius profile, we can solve for pressure by writing the more familiar

$$\int_{p_0}^{p} \frac{dp'}{p'} = -\int_{r_0}^{r} \frac{\mu m(r')g(r')}{k_BT} dr'. \tag{11}$$

Once either radius or pressure is determined, the result can be used with Equation 9 to find number density.

The procedure for generating a stellar occultation light curve from an atmospheric profile is as follows. First, either a temperature-pressure or temperature-radius profile is specified, along with a reference pressure p_0 at a reference radius r_0. Second, Equations 9, 10, and 11 are used to solve for remaining variables in the set $\{T, p, r, n\}$. Third, Equation

7 is used to calculate the refractivity at each radius $\nu(r)$. Fourth, bending angle $\theta(r)$ is calculated by integrating Equation 6. In the numerical implementation of this method, we use the classic Runge-Kutta method (Runge 1895). Fifth, $d\theta/dr$ is calculated numerically. Sixth, the observer positions y are provided and used to calculate the radius of close approach of each light ray $r(y)$ by interpolating the bending angle. Note that while the meaning of radius r is the same (distance from the center of the planet), the values calculated at this step are recast by the observer positions y instead of the input radius values from the first step. Last $d\theta/dr$ and θ are used to solve Equation 4 for flux at each observer point. The end product is the set of values $\{\phi, y, r, \theta\}$, where the ones of greatest interest are flux ϕ versus observer position y, because those are observed during a stellar occultation. Figure 4 is a flow chart showing the steps outlined here. For a more detailed description of how this procedure is implemented, the reader is directed to CE97.

3.2. *Comparison to Stellar Occultation Observations*

Our goal in using the forward modeling procedure is to compare an atmospheric profile to an observed stellar occultation. Here we discuss the tools we use to make that comparison, first for inspection and later with statistical rigor. In Section 5, we show the results of applying these comparison tools to Voyager 2 atmospheric profiles and the U0 occultation light curve.

In comparing a simulated light curve to an observed one, we explore whether or not the residuals are normally distributed. Photometric observations are Poisson distributed, but converge to normal by the central limit theorem with even a moderate number of counts.

In order to compare between these different observations, we have to be careful to adjust for the oblateness of Uranus. Using the figures reported by the IAU (Seidelmann et al. 2007) and the planetocentric sub-occultation latitudes reported in Elliot & Dunham (1979) and H87; S93, we calculate altitude above the 1 bar pressure level using Equation 6 in Withers & Jakosky (2017):

$$r_g^2 = \frac{a^2(1-f)^2(1+\tan^2\theta_c)}{(1-f)^2+\tan^2\theta_c},\tag{12}$$

where r_g is the 1 bar radius for a given latitude, a is the semi-major axis (equatorial 1 bar radius), $f = (a-b)/a$, b is the semi-minor axis (polar 1 bar radius), and θ_c is the planetocentric latitude. The IAU value of a is 25559 ± 4 km and b is 24973 ± 20 km, giving an ellipticity f of 0.02293 ± 0.00080, (Seidelmann et al. 2007; Lindal et al. 1987). Altitude is defined as $r - r_g$.

3.2.1. *Empirical Distribution Function*

The empirical distribution function is a cumulative distribution function for observed data (Feigelson & Babu 2012). We divide the residuals of the comparison between simulated light curves and observed light curves into ten blocks. Nine of these blocks are in the regions of the light curves away from the occultation, which serve as our baseline, and the last one contains the occultation. We then plot the empirical distribution functions for all ten blocks. This is a useful tool for inspection but does not provide statistical rigor. Therefore, we do not rely on it to draw conclusions, only to support results found with the methods discussed subsequently.

3.2.2. *Quantile-Quantile Plot*

A Quantile-Quantile (Q-Q) plot shows the quantiles of two distributions plotted against each other. Typically the quantiles of a theoretical distribution (e.g., normal) are plotted on the abscissa while those of the experimental data are plotted on the ordinate. A Q-Q plot includes a straight line, which represents total agreement between the quantiles, with a user-specified confidence interval. If at any point, the quantiles fall outside the confidence interval, it can be concluded that the observed data are likely drawn from a distribution different than the theoretical distribution. A Q-Q plot is commonly used by statisticians upon initial exploration of a dataset to determine which distribution best approximate the data. We include Q-Q plots here for a similar purpose and show the results of these in Section 5. Another useful aspect of a Q-Q plot is the ability to determine where in the distributions (e.g., center, tails) the observed quantiles diverge most strongly from the theoretical quantiles (Feigelson & Babu 2012).

3.2.3. *Anderson-Darling Test*

The Anderson-Darling (A-D) test is a non-parametric test of the null hypothesis that data are drawn from a given continuous probability distribution (Anderson & Darling 1954). The A-D statistic given in Equation 13 is calculated

by summing the weighted square of the differences of the two distributions at each data point. If the A-D statistic exceeds the critical value for a given choice of confidence, then we reject the null hypothesis and conclude that the data are not drawn from the given distribution (usually a normal distribution). If the A-D statistic does not exceed the critical value, we fail to reject the null hypothesis and conclude that the data are drawn from the given distribution (Corder & Foreman 2011).

$$A^2 = n \int_{-\infty}^{\infty} \frac{(F_n(x) - F(x))^2}{F(x)\,(1 - F(x))} dF(x), \tag{13}$$

where n is the size of the sample, F is the hypothesis distribution (normal), and F_n is the sample empirical distribution. The A-D test converges to the Cramer-von Mises test if the weighting function (the denominator in Equation 13) is everywhere 1. The effect of the weighting function in the A-D test is to place more emphasis on the tails of the distributions, where most distributions are small, making it difficult to determine variation. The A-D test differs from the commonly-used Kolmogorov-Smirnov (K-S) test, in that the K-S test statistic is the maximum absolute distance between the two distributions. By reporting only the maximum distance, the K-S test, again, is less sensitive to the tails of the distribution than the A-D test. Results from the empirical distribution function and Q-Q plots motivated our choice of the A-D test and not the Cramer-von Mises or K-S tests (Feigelson & Babu 2012).

In this work, we use the A-D test of normality to test the null hypothesis that the residuals of comparing a simulated stellar occultation to an observed occultation are normally distributed. That is, the null hypothesis is that the simulated occultation matches the observed stellar occultation.

4. STELLAR OCCULTATION PROCESSING

The method of processing a stellar occultation light curve was developed more than half a century ago and improved over the decades following. See Sicardy (2022) for a comprehensive review of these developments. Baum & Code (1953) were the first to process an occultation (by Jupiter) and did so by fitting an isothermal atmospheric profile to the light curve, returning a single temperature measurement. Kovalevsky & Link (1969) were the first to develop the procedure of "inversion," which converts each flux measurement into density, pressure, and temperature. They used and further developed a mathematically-similar solution that had been developed for radio occultations (Fjeldbo & Eshleman 1965; Fjeldbo et al. 1971). Significant improvements in this method were made during the 1970s (Vapillon et al. 1973; Wasserman & Veverka 1973; French et al. 1978), including early efforts to produce uncertainties on the resulting atmospheric properties.

The modern approach to processing a stellar occultation was provided in Elliot & Young (1992) and Elliot et al. (2003). Elliot & Young (1992) derived the first step in this procedure, which is to fit the upper portion of the occultation light curve to a simple atmospheric model. The model provides the necessary boundary conditions for the Elliot et al. (2003) inversion procedure. One can imagine a variety of models being used for this purpose but due to its simplicity and ease of computation, an isothermal model has been used nearly universally. Though not heavily used, Elliot & Young (1992) also derives a non-isothermal power-law model of the form

$$T(r) = T_0 \left(\frac{r}{r_0} \right)^b, \tag{14}$$

where the power-law exponent b is called the thermal "gradient." In Section 4.1.2, we explain how we use this non-isothermal model to provide boundary conditions instead of an isothermal model.

Elliot et al. (2003) derived the most advanced version of the inversion procedure, which has notable improvements over its predecessors in its applicability to all atmospheres (terrestrial, giant, hazy) and its uncertainty analysis. In short, this procedure is the reverse of the CE97 forward modeling procedure. We begin with observed, normalized stellar flux ϕ and wish to infer the atmospheric properties. In particular, flux is a function of the projected observer distance from the center of the planet $\phi(y)$. (See Section 3 for more details on the definition of y). A integral relationship exists between the radius of close approach of each light ray r and the projected observer position y:

$$r = \left\{ y^2 + 2 \int_y^{\infty} [1 - \phi(y')]\, y' dy' \right\}^{1/2}. \tag{15}$$

This integral is evaluated numerically from y to some y_b specified by the boundary condition model fit and analytically from y_b to ∞.

Using Equation 2, a bending angle θ can be calculated from each pair of y and r values. (See Figure 3 for the visual relationship between these variables). Equation 6 relates the bending angle θ to the local atmospheric refractivity ν, however, we need to invert this equation to solve for ν. That solution is given via an Abel transform (Abel 1826) and is whence "inversion" derives its name. The inverse of Equation 15 is given by

$$\nu(r) = -\frac{1}{\pi} \int_r^\infty \frac{\theta(r')}{\sqrt{r'^2 - r^2}} dr', \tag{16}$$

in which variables from Equations 2 and 6 have been substituted. This is further modified using integration by parts to avoid the infinite integrand at $r' = r$. For further detail, the reader is directed to Section 2 of Elliot et al. (2003). Refractivity is related to number density, temperature, and pressure using Equations 7, 9, and 11.

The inversion procedure determines uncertainties by solving the covariance matrices step-by-step for all variables. Because inversion is iterative and integrative, the values are highly correlated. For the details on the numerical implementation of this procedure, the reader is directed to Sections 3 and 4 of Elliot et al. (2003).

4.1. *Critical Improvements to Processing*

In performing this analysis, we identified two critical shortcomings with the existing procedure for performing occultation light curve analysis: the approach to binning flux measurements and the choice of boundary condition. It is often necessary to perform some binning before inversion but the Elliot et al. (2003) approach described below results in systematic errors in the inversion products. Regarding the boundary condition, the traditional approach has been to use an isothermal atmospheric model to determine boundary conditions, which can be problematic when the goal is to test whether or not an atmosphere is approximately isothermal. In this subsection, we first describe the origin of these two issues, then our approaches to solving them, and last demonstrate the solution with examples.

4.1.1. *Ratchet Binning*

During a stellar occultation, the flux from the star must always be positive. Even while completely behind the planet, some stellar flux is always refracted around the planet. Exploratory forward modeling indicates that this is usually in the range of 0.1% of the total stellar flux. However, due to photon noise (scintillation and read noise to a lesser extent), there are often many measurements of negative stellar flux as an occultation progresses. Negative stellar flux has two problems. First, and most obviously, it is unphysical. Second, it produces a degeneracy in close approach radius. Using Equation 15, we solve for the close approach radius of each ray r using known observer position y and flux ϕ. Since y is decreasing, dy is negative, which means the integrand in that equation is strictly negative. However, when flux is negative, the integrand becomes positive, which means that we find a larger close approach radius r for that ray than the previous ray. This implies that the rays were received out of order, which we call "ray crossing." There is a degeneracy in this measurement because it's possible the ray probed a higher altitude or that the ray probed a lower altitude with strong turbulence at Uranus that strongly increased the bending and also delayed the arrival of the ray. Prohibiting negative flux is necessary to alleviate this issue.

We cannot simply remove the negative flux measurements. Instead, Elliot et al. (2003) devised the approach of averaging the minimum number of adjacent flux measurements to each negative value to return a positive averaged value. This has the benefit of maximizing the vertical resolution. It also has a serious drawback: for high-resolution data, the result of averaging away negative flux values returns barely positive flux measurements that span a large bin interspersed with individual positive flux measurements without any binning. There is a stark difference between the sizes of subsequent bins. In solving Equation 15 numerically, Elliot et al. (2003) calculates Δy as

$$(\Delta y)_i = (y_{i+1} - y_{i-1})/2, \tag{17}$$

where the subscript i corresponds to the ith bin (see Equation 33 of Elliot et al. (2003)). In this equation, the width of the bin depends on the positions of the adjacent bins. The center of each bin y_i is found by referencing the edges of the bin

$$y_i = (y_{i,0} + y_{i,-1})/2, \tag{18}$$

where $y_{i,0}$ is the first entry in the ith bin and $y_{i,-1}$ is the last entry.

Combining Equations 17 and 18, we find

$$(\Delta y)_i = (y_{i+1,0} + y_{i+1,-1} - y_{i-1,0} - y_{i-1,-1})/4, \tag{19}$$

where $y_{i+1,0}$ is the first entry in the previous bin, $y_{i+1,-1}$ is the last entry in the previous bin, $y_{i-1,0}$ is the first entry in the subsequent bin, and $y_{i-1,-1}$ is the last entry in the subsequent bin. The numerical implementation of inversion requires calculating the width of the bin by referencing the edges of the previous and subsequent bins. This works fine when the bins are roughly the same size, but it creates significant problems when they are not. When the previous and subsequent bins are significantly different in size than the current bin, the calculated $(\Delta y)_i$ using Equation 19 is significantly larger in magnitude (more negative) than the true value.

This error propagates throughout the inversion procedure. Equation 15 returns smaller r values, which are fed into Equation 3 to solve for bending angles θ, which have larger magnitude. Equation 16 (after the Abel transform of Equation 6) is used to find refractivity ν, which is larger due to θ values of greater magnitude. Fed with larger refractivity values, Equation 7 returns larger number density and Equation 8 returns lower pressure at a given radius. Last, and most importantly, Equation 9 finds higher temperatures. To summarize, the minimum-positive-binning procedure employed in Elliot et al. (2003) results in systematically higher temperature values. It's important to note that this becomes a problem only at high vertical resolution. Lower vertical resolution light curves already have a universal binning built in, which diminishes the error introduced by widely different adjacent bin sizes. However, as one of the motivations of reprocessing the U0 occultation is to use the full resolution data, as mentioned in Section 1, we need to resolve this issue.

Our solution is a procedure called "ratchet binning." In this procedure, we still average negative flux with sufficient adjacent points to become positive, but we do not permit the averaging to decrease thereafter. For example, if a negative flux value requires averaging with two adjacent positive values to become positive, the ratchet is set to a minimum bin size of three from there onward. This means that the amount of binning increases gradually with decreasing flux. The upside of this method is that all adjacent bins are nearly the same size, ameliorating the above problem. The downside of this method is that the resolution is lower at the bottom of the profile than otherwise.

Figure 5 shows two examples. For Figure 5a, we generated an isothermal light curve with a temperature of 76 K and added either 3% or 20% random noise, with the latter approximating the U0 noise profile. For Figure 5b, we generated a light curve with a thermal gradient approximating that of Uranus as shown in Figure 1 and added either 3% or 20% random noise. We then inverted both synthetic light curves using the original and ratchet binning methods, and compare them back to the inputs in these figures.

Looking at Figure 5, we see that in both subfigures, the Elliot et al. (2003) binning procedure results in significantly higher temperatures toward the bottom of the profile. The error is much worse with the 20% noise case. For ratchet binning, by contrast, the deviations are much smaller and predominantly due to noise. Even in the 20% case, ratchet binning has errors of only about 30 K at the bottom of the profiles, compared with hundreds of K for the older binning procedure.

It's important to note that most of the published profiles from stellar occultation observations made decades ago (including the U0 observations) are not subject to the degree of systematic errors shown in Figure 5, because they were conducted at much lower vertical resolution due to limitations in computational power.

4.1.2. *Thermal Gradient Boundary Condition*

The other major improvement to the occultation processing procedure undertaken here is the atmospheric model used to fit to the light curve for the purpose of generate boundary conditions. At the time of the U0 occultation, the approach to boundary conditions was to fit an isothermal atmospheric model to the portion of the light curve between 1.0 and 0.7 normalized flux (the upper portions) (Elliot & Dunham 1979; Dunham et al. 1980). In particular, they used the isothermal model developed by Baum & Code (1953). The boundary conditions provide the first point in the retrieved profile, after which inversion is run on flux from about 0.7 to 0.0 flux.

As mentioned in Section 4, Elliot & Young (1992) developed the current model fitting produced, and generalized the model to include a possible non-isothermal, thermal gradient power law given in Equation 14. With the power-law exponent b set to 0, this becomes an isothermal model, but allowing b to take on any value makes it possible to retrieve a non-isothermal fit from the light curve. (See Sections 4–6 of Elliot & Young (1992) for the full derivation of the model.) This model was not available in 1977 when the U0 event was observed.

In this work, we choose to use the thermal gradient model in Equation 14 for generating boundary conditions because we endeavor to test the hypothesis generated from Voyager 2 observations that Uranus has a strong thermal gradient in the lower thermosphere. In Section 6 we compare the results of this work using the non-isothermal, thermal gradient model to what we would have found using the isothermal model.

5. FORWARD MODELING RESULTS: VALIDATION ON U0

In the previous sections we have explained the procedures used to answer the motivating questions for this work presented in Section 1. In this section and the subsequent sections, we demonstrate these procedures using the U0 occultation and show the detailed results. In Paper II, we apply these procedures to many archival stellar occultations and seek to formally answer the motivating questions.

We applied the CE97 forward modeling procedure described in Section 3 to the H87 and S93 atmospheric profiles, converting them into simulated Earth-based stellar occultation light curves. Unlike CE97, we did not assume a homogeneous atmosphere and instead used the varying atmospheric composition with altitude published along with each Voyager profile. For those profiles, an 85% H_2 and 15% He atmosphere rapidly transitions with altitude into an H_2-dominated atmosphere. See Section 3 of S93 for a detailed description of the mixing ratio used.

Figure 6 shows the comparison of the U0 light curve to simulated light curves from H87 and S93 using the forward modeling procedure. Below each light curves, we plot residuals for the portions of the light curves above the region where spikes, which are caused by atmospheric turbulence at Uranus, dominate. The upper two rows (Figure 6a, Figure 6b, Figure 6c, and Figure 6d) show the U0 ingress (black, left) and egress (black, right) compared with H87 stellar ingress / egress (red) and H87 solar ingress (purple). Looking at the light curves (Figure 6a and Figure 6b), we can see that the H87 profiles have a slower turnover than the U0 light curves at around 600 km altitude. From the residuals (Figure 6c and Figure 6d), the H87 Voyager profiles align with the U0 light curve above about 700 km but begin to diverge significantly between 400 and 700 km. This is the first indication that these profiles of the atmosphere of Uranus are fundamentally inconsistent with the U0 observation.

The bottom two rows (Figure 6e, Figure 6f, Figure 6g, and Figure 6h) show the U0 ingress (black, left) and egress (black, right) compared with S93 stellar ingress (blue), S93 stellar egress (orange), and S93 solar ingress (green). Looking at the light curves (Figure 6e and Figure 6f), we can see that the S93 profiles have a much slower turnover than the U0 light curves at around 600 km altitude. From the residuals (Figure 6g and Figure 6h), the three S93 Voyager profiles align with the U0 light curve above about 800 km but begin to diverge significantly between 400 and 800 km. This is another indication that these profiles of the atmosphere of Uranus are fundamentally inconsistent with the U0 observation. Note in the region around 600 km, the S93 profiles are noticeably farther from U0 than the H87 profiles.

Figures 7 and 8 show the results of the empirical distribution function test outlined in Section 3.2 for the H87 and S93 profiles, respectively. The residuals shown in Figure 6c, 6d, 6g, and 6h are divided into ten blocks, with approximate block edges every 500 km starting at an altitude of approximately 500 km. The block from 500 to 1000 km includes the beginning of the occultation and the remaining nine of the blocks include only baseline residuals. (Note that most of the blocks are off the right edge of the subfigures in Figure 6). Each subfigure in Figures 7 and 8 shows ten empirical cumulative distribution functions for each of the ten blocks of residuals. The one distribution corresponding to the block containing the occultation is shown in the same color used in Figure 6.

In the top row of Figure 7 (U0 ingress), the occultation has an obviously different distribution from the baselines in both tails (large and small quantiles). In the bottom row (U0 egress), the occultation has an obviously different distribution only at the larger tail. This implies that the U0 egress agrees more closely with the Voyager profiles than the ingress does, while still standing out. For Figure 8, the results are similar. The top row (U0 ingress) occultation has a more obviously different distribution than the baselines than the bottom row (U0 egress) does. In most cases, the disagreements between occultation and baseline in Figure 8 are greater than those in Figure 7, which indicates that the U0 light curve more closely agrees with the H87 profiles than the S93 profiles, while still not agreeing with either.

Figures 9 and 10 show quantile-quantile plots for each of the ten residuals from Figure 6c, 6d, 6g, and 6h, following the procedure outlined in Section 3.2. The theoretical quantiles are from a normal distribution and the ordered quantiles are from the occultation data. The solid red line is the expected result if the data were drawn perfectly from a normal distribution with dashed lines represent the 99.99% confidence intervals on that null hypothesis.

All ten subfigures in Figures 9 and 10 show many points lying outside the confidence intervals, especially at the tails of the distribution. Notice that the U0 ingress data (top rows of Figures 9 and 10) fall outside the confidence intervals more than the U0 egress data (bottom rows). This supports a similar observation from Figures 7 and 8. In all 10 cases, Figures 9 and 10 indicate to a high degree of statistical confidence (>99.99%) that these residuals are not normally distributed. For comparison, Figure 11 shows a quantile-quantile plot for a baseline portion of one of the residuals away from the occultation. These points, by contrast to Figures 9 and 10, lie entirely within the

90% confidence intervals. That is, the baseline portions of these residuals *are* normally distributed. Note that the 90% confidence interval is actually a stricter requirement in this case, because it lowers the bar to be considered non-normally distributed. However, the data fail to clear even this lower bar, meaning the baseline data are normally distributed and the experimental data are non-normally-distributed.

The last method used to compare the U0 light curve to the simulated light curve from Voyager 2 measurements is the Anderson-Darling (A-D) test of normality, explained in Section 3.2.3. For this test, our null hypothesis is that *the occultation residuals are drawn from a normal distribution*. Table 2 shows the results of the A-D test, where the first two rows are for baseline data and the bottom two rows are for occultation data. Even if we find the occultation data to be non-normally distributed, we need the residual data to be normally distributed to reject the null hypothesis. Each entry in the table is the A-D statistic value for that sample. The critical value for 99% confidence is indicated below.

Looking at the first two rows, we see that the A-D statistics for H87 and S93 profile baseline data are all below the critical value. This indicates that we cannot reject the null hypothesis of a normal distribution at the 99% confidence level. Looking at the bottom two rows, we see that the A-D statistics for H87 and S93 profile occultation data are all above the critical value. This indicates that we can reject the null hypothesis of a normal distribution at the 99% confidence level. That is, the baseline H87 and S93 profiles are consistent with the U0 light curve but the occultation H87 and S93 profiles are inconsistent with the U0 light curve at the 99% confidence level.

In addition, note that the A-D statistics for the S93 model residuals exceed those of H87. This corroborates what we noted from Figure 6. Furthermore, the A-D statistics for the U0 ingress profiles (row 3 in Table 2) exceed those for the U0 egress profiles (row 4), which corroborates what we noted from Figures 7, 8, 9, and 10. In short, all of the Voyager 2 profiles strongly disagree with the U0 observation at significance well above 99%, but the H87 profiles are slightly closer than the S93 profiles and both better agree with U0 ingress than egress.

6. REPROCESSING RESULTS: VALIDATION ON U0

In the previous section we forward modeled the H87 and S93 Voyager 2 profiles into stellar occultation light curves, finding that those light curves are inconsistent with the observed U0 light curve. In this section, we demonstrate the stellar occultation processing techniques described in Section 4 on the U0 light curves by creating reliable temperature profiles. In doing so, we validate our improvements to model fitting and inversion before applying them to many other occultation observation in Paper II.

Figure 12 shows the normalized U0 channel 2 light curve in black overlaid with Elliot & Young (1992) thermal gradient models in blue. These light curves were binned from the initial resolution of 0.01 s to 0.1 s for the purpose of this figure only. We fit the gradient model to the portions of the U0 light curve on ingress and egress above where turbulence creates spikes, visible at radii $\lesssim$450 km. Table 3 shows the parameters of this fit, which are then used to generate upper boundary conditions for inversion. We chose to begin inversion around a flux level of 0.9 for this light curve.

Figure 13 shows the primary result of inversion: temperature profiles for the three channels and comparison to the original analysis of the channel 2 data in Elliot & Dunham (1979). These profiles are plotted as temperature versus pressure, with approximate altitude above the 1 bar pressure level as a secondary ordinate. Shaded regions of the profiles indicate the 1σ uncertainties. These profiles span pressure levels of about 0.3μbar–40μbar, corresponding to approximately 600–350 km above the 1 bar pressure level.

Aside from the very bottom of the ingress profile, all three channels agree within their uncertainty regions. On the ingress profiles, all three reanalysis channels and the original channel 2 show the same local temperature maximum of about 135 K at 10 μbar and then cool to a minimum of about 100 K at 1.5 μbar. From there to the top of the profiles, temperatures increases monotonically, but increase more strongly for the reprocessed profiles. To the top of the original, however, these remain within the overlapping 1σ error regions. The reprocessed profiles show temperatures around 180 K at the top of the profiles, which are the boundary condition values.

On the egress profiles, all four show a local temperature maximum at about 10 μbar but it is much less pronounced than the ingress maximum at that pressure level. The reprocessed profiles show a weak minimum of about 130 K at approximately 2 μbar, different from the original, which continues to decrease with altitude to about 75 K at 0.3 μbar pressure level. The reprocessed profiles increase above 2 μbar up to about 180 K at the top of the profiles. In this case, unlike for ingress, the reprocessed and original profiles do not have any overlap in their uncertainty regions. The reprocessed profiles for all channels have much higher vertical resolution than the original profiles, which can be

observed, for example, in the small-scale variation visible on the three reprocessed egress profiles at around 10 μbar pressure but not on the original egress profile.

In Section 4.1.2, we described and illustrated the implications of using a thermal gradient boundary condition. Here we show the implications for the U0 reprocessing. Figure 14 shows the temperature-pressure profile for channel 2 using a thermal gradient boundary condition (as in Figure 13), the profile using an isothermal boundary condition, and the original profile. The isothermal boundary condition enforces a profile closer to isothermal at the top, but is quickly swamped by inversion and converges to the thermal gradient result within about 1 scale height. Notably, the reprocessed isothermal boundary condition profile agrees more closely with the reprocessed thermal gradient boundary condition profile in both ingress and egress, and not with the original profile. So while using the non-isothermal, thermal gradient model improves performance at the top of these profiles, the increase in vertical resolution compared to the original analysis influences the entire profile.

7. PRELIMINARY INTERPRETATION & DISCUSSION

In this work (Paper I), we laid out two primary methods for analyzing stellar occultations: forward modeling and inversion with model fitting. We validated these methods and our improvements thereto using the 1977 U0 stellar occultation observation. In Section 5, we forward modeling the H87 and S93 Voyager 2 profiles to create simulated Earth-based occultation light curves that we compared to the observed U0 light curve. Our primary finding is that all 5 Voyager 2 light curves are inconsistent with the U0 observations at a confidence of >99%.

By comparing the Voyager 2 profiles directly to the U0 measurements using forward modeling, we don't have to invoke any of the assumptions or boundary conditions required for inverting the light curve. Having found that the Voyager 2 results are inconsistent with the U0 light curve, we applied an improved version of the model fitting and inversion procedures. We found in Section 6 that the U0 observations indicate temperatures slightly warmer than the original analysis in the ingress and moderately warmer than the original in the egress. At the tops of these profiles, we find moderately warmer temperatures for both ingress and egress.

We now compare the temperature profiles derived from reprocessing the U0 observation to the Voyager 2 profiles. Figure 15 follows the comparison of Figure 1 with the new U0 temperature-pressure profiles derived in this work. In comparison to Figure 1, Figure 15 shows temperatures closer to the H87 Voyager 2 UV solar occultation results. In particular, the H87 UV stellar point at 200 K and 1 μbar is much closer to the reprocessed U0 results than to the original shown in Figure 1. UV occultation points at 10 μbar and about 50 μbar remain within agreement of the U0 profiles.

On the other hand, the H87 points in the middle thermosphere, at about 500 K and 0.1–1 μbar, remain starkly in tension with the stellar occultation results. It's worth pointing out that the H87 profile is in tension with itself; compare the UV stellar occultation point at 200 K and 1 μbar with the UV solar occultation point at 475 K and 1 μbar. As explained in Section 1, the points around 500 K are from the H_2 lines, which are the most difficult to process of these observations. In addition, while the reprocessed stellar occultation profiles are slightly closer to the S93 models, they remain in strong tension at all altitudes. Considering the S93 models were fit to the H87 data, this is unsurprising.

Bishop et al. (1990) produced atmospheric models for Uranus with the aim of smoothly connecting the radio occultation profiles in the troposphere to the lower points of the H87 in the stratosphere (pressures greater than about 0.02 mbar). Figure 5 in Bishop et al. (1990) shows these composite profiles, which follow the radio occultation profiles until about 10 mbar, become warmer than the radio occultation profiles by about 15 K from 2 mbar up to 0.4 mbar and then approach temperatures of 115–145 K at 0.02 mbar. While this composite profiles does not have significant bearing on our findings here, 115–145 K at 0.02 mbar agree with our egress profiles shown in Figure 15.

Last, we note the apparent detection of a clear mesopause at T = 100 $\pm$ 8 K and p = 2×10^{-3} mbar from the occultation ingress shown in Figure 13. The egress shows a less striking mesopause, with T = 120 $\pm$ 20 K at the same pressure level as in the ingress.

8. PRELIMINARY CONCLUSIONS

In this work (Paper I) we applied two procedures to the U0 stellar occultation: forward modeling and inversion with model fitting. The former enabled us to forward model the Uranus atmospheric profiles created from Voyager 2 measurements (H87; S93) into stellar occultation light curves that we compared with the U0 light curve. Using three comparison methods, we find that the H87 and S93 profiles are inconsistent with the U0 light curve to a high degree of

statistical confidence. The latter method, occultation processing, resulted in temperature-pressure profiles that further support the finding of inconsistency between U0 and Voyager 2 profiles, though these profiles also differed from the originally-published results (Elliot & Dunham 1979; Dunham et al. 1980) to a lesser degree.

Therefore, we conclude that the upper stratosphere and lower thermosphere of Uranus is not well-represented by the discrete H87 profiles and S93 atmospheric models, based on Voyager 2 UV occultation measurements. The points of about 500 K in the middle thermosphere are the most problematic of the Voyager 2 measurements. In some respects, this is unsurprising. H87 acknowledged that absorption features from the H_2 lines are the most difficult to process because Voyager 2 had low spectral resolution.

We offer preliminary answers to the motivating questions posed in Section 1. *Question 1: Are Earth-based stellar occultation temperature profiles consistent with Voyager 2 UV temperature profiles?* No, to a high degree of statistical confidence, the H87 and S93 profiles are inconsistent with the U0 observation. *Question 2: What is the upper atmospheric structure of Uranus?* Looking at Figure 15, the reliable Voyager 2 radio occultations show a gradually warming stratosphere around 100 K that connects to the bottom end of the reprocessed U0 occultation. This agrees with the lower points in the H87 and S93 profiles. The upper stratosphere (or perhaps mesosphere) has a temperature inversion but remains cool, between 100 and 140 K. The lower thermosphere shows a significant warming from about 1 μbar upward, at 150 to 200 K.

In Paper II, we will present the results of applying the analysis techniques discussed here to many more Uranus stellar occultations observed between 1977 and 1998 and we will synthesize those results to provide our final answers to these questions. Specifically, we will present efforts to investigate whether the temperature structure of Uranus varies with latitude, time of day, solar zenith angle, season, or other variables. We will compare our findings to those of Baron et al. (1989), which concluded that the stratosphere of Uranus warmed at a rate of roughly 8 K/year from 1977 to 1983. Young et al. (2001) identified a cooler temperature in 1998, indicating that the warming trend had reversed between 1983 and 1998. Our reprocessing effort will explore these claims and fill in the gap. We will also compare our results with detections of the H_3^+ ion, which have found a roughly 8 K / year decreasing thermospheric temperature since the early 1990s (Trafton et al. 1993; Melin et al. 2019; Melin 2020a). H_3^+ observations probe temperatures above the homopause, at pressure levels of roughly 10^{-4} to 10^{-8} mbar, which are just above the upper range of the profiles produced in this work (Moore et al. 2019). Furthermore, we will compare our findings with disk-integrated, ground based photometry (that probes the troposphere) spanning 1972–2016 (Lockwood 2019).

Last, in Paper II, we will discuss the impact of our findings on the energy balance of Uranus and the giant planet energy crisis. Given the known limitations of the Voyager 2 data and the findings of this work, we intend to offer a revised representative profile as part of our findings.

REFERENCES

Abel, N. H. 1826, J. Reine Angew. Math, 1, 153

Anderson, T. W., & Darling, D. A. 1954, Journal of the American statistical association, 49, 765

Baron, R. L., French, R. G., & Elliot, J. L. 1989, Icarus, 78, 119, doi: 10.1016/0019-1035(89)90073-0

Baum, W. A., & Code, A. D. 1953, AJ, 58, 108, doi: 10.1086/106829

Bishop, J., Atreya, S. K., Herbert, F., & Romani, P. 1990, Icarus, 88, 448, doi: 10.1016/0019-1035(90)90094-P

Bishop, J., Atreya, S. K., Romani, P. N., et al. 1995, in Neptune and Triton (Univ. Arizona Press Tucson), 427–487

Born, M., & Wolf, E. 2013, Principles of optics: electromagnetic theory of propagation, interference and diffraction of light (Elsevier)

Borucki, W. J., Koch, D., Basri, G., et al. 2010, Science, 327, 977, doi: 10.1126/science.1185402

Broadfoot, A. L., Sandel, B. R., Shemansky, D. E., et al. 1977, SSRv, 21, 183, doi: 10.1007/BF00200850

Catling, D. C. 2015, in Treatise on Geophysics, ed. G. Schubert, 429–472, doi: 10.1016/B978-0-444-53802-4.00185-8

Chamberlain, D., & Elliot, J. 1997, PASP, 109, 1170, doi: 10.1086/133992

Corder, G., & Foreman, D. 2011, Nonparametric Statistics for Non-Statisticians: A Step-by-Step Approach (Wiley). https://books.google.com/books?id=T3qOqdpSz6YC

Dunham, E., Elliot, J. L., & Gierasch, P. J. 1980, ApJ, 235, 274, doi: 10.1086/157631

Elliot, J. L., & Dunham, E. 1979, Nature, 279, 307, doi: 10.1038/279307a0

Elliot, J. L., Dunham, E., & Mink, D. 1977a, Nature, 267, 328, doi: 10.1038/267328a0

Elliot, J. L., French, R. G., Dunham, E., et al. 1977b, ApJ, 217, 661, doi: 10.1086/155612

Elliot, J. L., Glass, I. S., French, R. G., & Kangas, J. A. 1987, Icarus, 71, 91, doi: 10.1016/0019-1035(87)90165-5

Elliot, J. L., Person, M. J., & Qu, S. 2003, AJ, 126, 1041, doi: 10.1086/375546

Elliot, J. L., Veverka, J., & Millis, R. L. 1977c, Nature, 265, 609, doi: 10.1038/265609a0

Elliot, J. L., & Young, L. A. 1992, AJ, 103, 991, doi: 10.1086/116121

Eshleman, V. R., Tyler, G. L., Anderson, J. D., et al. 1977, SSRv, 21, 207, doi: 10.1007/BF00200851

Feigelson, E. D., & Babu, G. J. 2012, Modern statistical methods for astronomy: with R applications (Cambridge University Press)

Fjeldbo, G., & Eshleman, V. R. 1965, J. Geophys. Res., 70, 3217, doi: 10.1029/JZ070i013p03217

Fjeldbo, G., Kliore, A. J., & Eshleman, V. R. 1971, AJ, 76, 123, doi: 10.1086/111096

Fletcher, L. N., Helled, R., Roussos, E., et al. 2020, Planetary and Space Science, 105030

French, R. G., Elliot, J. L., Dunham, E. W., et al. 1983, Icarus, 53, 399, doi: 10.1016/0019-1035(83)90205-1

French, R. G., Elliot, J. L., & Gierasch, P. J. 1978, Icarus, 33, 186, doi: 10.1016/0019-1035(78)90032-5

French, R. G., Elliot, J. L., Sicardy, B., Nicholson, P., & Matthews, K. 1982, Icarus, 51, 491, doi: 10.1016/0019-1035(82)90142-7

French, R. G., Jones, T. J., & Hyland, A. R. 1987, Icarus, 69, 499, doi: 10.1016/0019-1035(87)90019-4

Fulton, B. J., & Petigura, E. A. 2018, AJ, 156, 264, doi: 10.3847/1538-3881/aae828

Herbert, F., Sandel, B. R., Yelle, R. V., et al. 1987, J. Geophys. Res., 92, 15093, doi: 10.1029/JA092iA13p15093

Koskinen, T. T., Sandel, B. R., Yelle, R. V., et al. 2015, Icarus, 260, 174, doi: 10.1016/j.icarus.2015.07.008

Kovalevsky, J., & Link, F. 1969, A&A, 2, 398

Lindal, G. F., Lyons, J. R., Sweetnam, D. N., et al. 1987, J. Geophys. Res., 92, 14987, doi: 10.1029/JA092iA13p14987

Lockwood, G. W. 2019, Icarus, 324, 77, doi: 10.1016/j.icarus.2019.01.024

Marley, M. S., & McKay, C. P. 1999, Icarus, 138, 268, doi: 10.1006/icar.1998.6071

Melin, H. 2020a, Philosophical Transactions of the Royal Society of London Series A, 378, 20190478, doi: 10.1098/rsta.2019.0478

—. 2020b, Nature Astronomy, 4, 837, doi: 10.1038/s41550-020-1167-3

Melin, H., Fletcher, L., Stallard, T., et al. 2019, Philosophical transactions of the Royal Society A, 377, 20180408

Millis, R. L., Wasserman, L. H., & French, R. G. 1987, Icarus, 69, 176, doi: 10.1016/0019-1035(87)90012-1

Moore, L., Melin, H., O'Donoghue, J., et al. 2019, Philosophical Transactions of the Royal Society of London Series A, 377, 20190067, doi: 10.1098/rsta.2019.0067

Mueller-Wodarg, I. C. F., Strobel, D. F., Moses, J. I., et al. 2008, SSRv, 139, 191, doi: 10.1007/s11214-008-9404-6

NASEM. 2022

O'Donoghue, J., Moore, L., Bhakyapaibul, T., et al. 2021, Nature, 596, 54, doi: 10.1038/s41586-021-03706-w

Orton, G. S., Fletcher, L. N., Moses, J. I., et al. 2014, Icarus, 243, 494, doi: 10.1016/j.icarus.2014.07.010

Pearl, J. C., Conrath, B. J., Hanel, R. A., Pirraglia, J. A., & Coustenis, A. 1990, Icarus, 84, 12, doi: 10.1016/0019-1035(90)90155-3

Rowe-Gurney, N., Fletcher, L. N., Orton, G. S., et al. 2021, Icarus, 365, 114506, doi: 10.1016/j.icarus.2021.114506

Runge, C. 1895, Mathematische Annalen, 46, 167

Seidelmann, P. K., Archinal, B. A., A'Hearn, M. F., et al. 2007, Celestial Mechanics and Dynamical Astronomy, 98, 155, doi: 10.1007/s10569-007-9072-y

Sicardy, B. 2022, arXiv e-prints, arXiv:2206.06236, doi: 10.48550/arXiv.2206.06236

Sicardy, B., Combes, M., Brahic, A., et al. 1982, Icarus, 52, 454, doi: 10.1016/0019-1035(82)90006-9

Sicardy, B., Combes, M., Lecacheux, J., et al. 1985, Icarus, 64, 88, doi: 10.1016/0019-1035(85)90040-5

Smith, G. R., Shemansky, D., Holberg, J., et al. 1983, Journal of Geophysical Research: Space Physics, 88, 8667

Stevens, M. H., Strobel, D. F., & Herbert, F. 1993, Icarus, 101, 45, doi: 10.1006/icar.1993.1005

Sumi, T., Udalski, A., Bennett, D. P., et al. 2016, ApJ, 825, 112, doi: 10.3847/0004-637X/825/2/112

Taylor, G. E. 1973, Journal of the British Astronomical Association, 83, 352

Trafton, L. M., Geballe, T. R., Miller, S., Tennyson, J., & Ballester, G. E. 1993, ApJ, 405, 761, doi: 10.1086/172404

Vapillon, L., Combes, M., & Lecacheux, J. 1973, A&A, 29, 135

Vervack, R. J., & Moses, J. I. 2015, Icarus, 258, 135, doi: 10.1016/j.icarus.2015.06.007

Wasserman, L. H., & Veverka, J. 1973, Icarus, 20, 322, doi: 10.1016/0019-1035(73)90009-2

Winn, J. N., & Fabrycky, D. C. 2015, ARA&A, 53, 409, doi: 10.1146/annurev-astro-082214-122246

Withers, P., & Jakosky, B. M. 2017, Journal of Geophysical Research (Space Physics), 122, 802, doi: 10.1002/2016JA023470

Yelle, R. V., Doose, L. R., Tomasko, M. G., & Strobel, D. F. 1987, Geophys. Res. Lett., 14, 483, doi: 10.1029/GL014i005p00483

Young, L. A., Bosh, A. S., Buie, M., Elliot, J. L., & Wasserman, L. H. 2001, Icarus, 153, 236, doi: 10.1006/icar.2001.6698
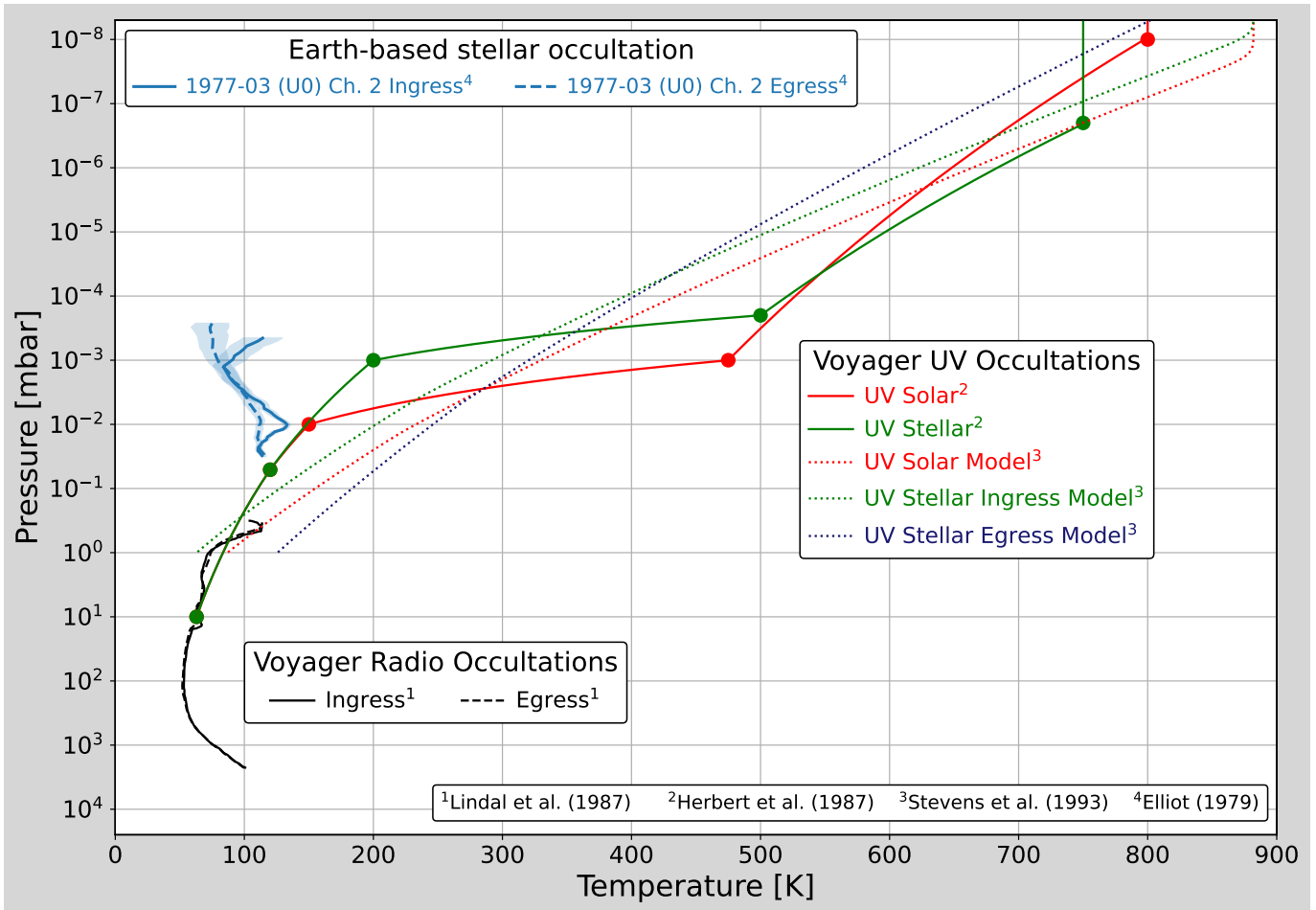
Figure 1. Comparison of the temperature-pressure profiles produced by three archival remote-sensing measurements: Voyager 2 radio occultations, Voyager 2 UV stellar and solar occultations, and the U0 Earth-based stellar occultation. The radio occultations are shown in black in the lower atmosphere. The H87 retrieved temperatures from the Voyager UV occultations are shown in green and red points, connected by thermal gradients. The S93 models fit to the H87 data are shown in red, green, and navy dotted lines. The U0 occultation is shown in blue with shaded 1σ uncertainty. Note the large discrepancy between the Earth-based temperatures and Voyager 2 temperatures, especially at the 10^{-3} mbar pressure level.
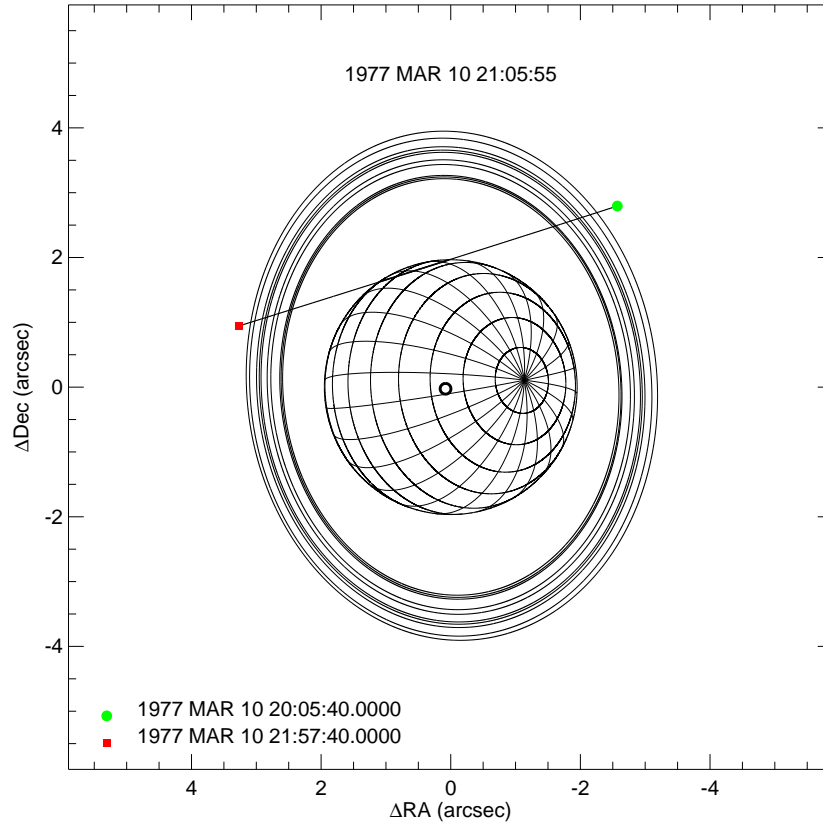
Figure 2. The orientation of Uranus as seen from Earth during the U0 occultation. The line is the projected path of the occultation star ("occultation chord") on the disk of Uranus, moving from green circle (right) to red square (left). The open circle indicates the location of the sub-solar point. As shown, the obliquity of the planet makes the occultation path almost entirely equatorial.
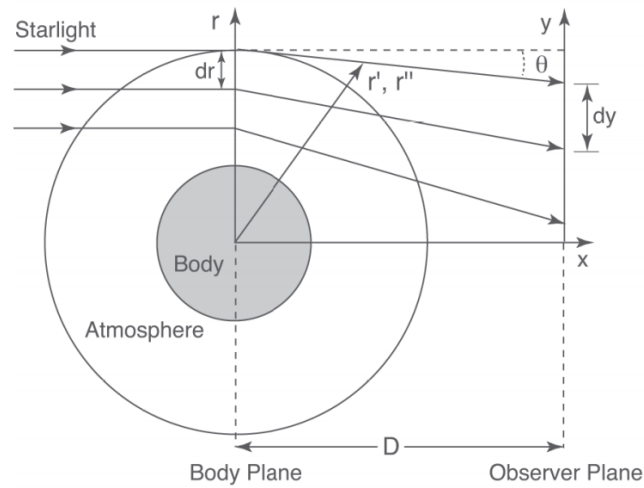
Figure 3. A diagram showing the geometry of an occultation. Parallel rays of time-separated starlight enter from the left and are bent by an angle θ as a function of their close approach distance to the planet r. They are received at the observer position y, distance D from the planet. r' and r'' are dummy variables. Notice that the distance scale (dy) is expanded in the plane of the observer compared to the actual dimensions at the planet (dr). Figure 1 from Elliot et al. (2003).
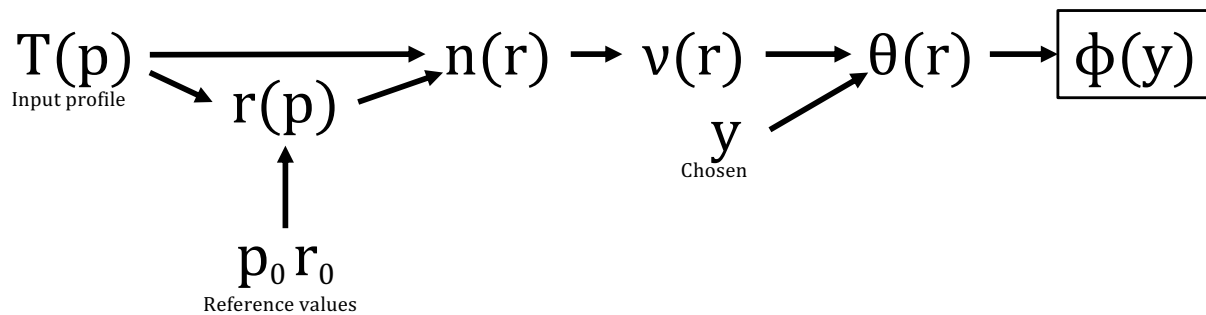
Figure 4. Flow chart showing the steps of forward modeling. For the definition of each symbol, see the text. Notice that temperature profile, impact parameter (y), and reference values are the only independent inputs to the process. For definitions of these symbols, see Section 3.1.
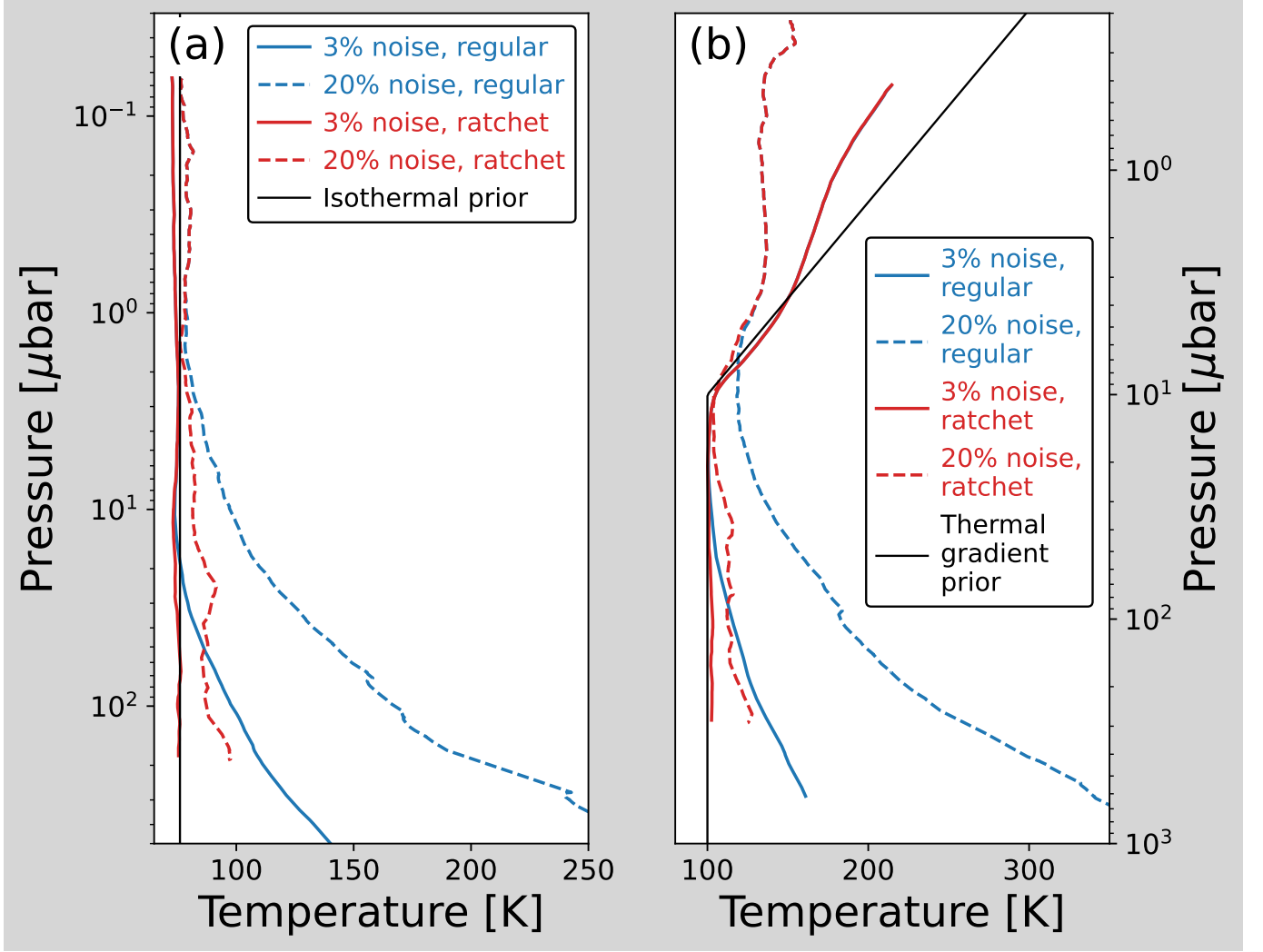
Figure 5. An example of the difference between using the Elliot et al. (2003) minimum-binning approach and our ratchet binning approach. In (a), we show an isothermal profile and in (b), a profile more realistic for Uranus (both in black). Each profile was simulated into light curves and then processed back into profiles. The light curves that were processed using minimum binning as in Elliot et al. (2003) are shown in blue and those processed using ratchet binning are shown in red. Light curves with 3% random noise are shown in solid lines and those with 20% random noise are shown in dashed lines. The minimum-binning procedure creates large, systematic errors that are not created using ratchet binning, leading us to use ratchet binning in this work.
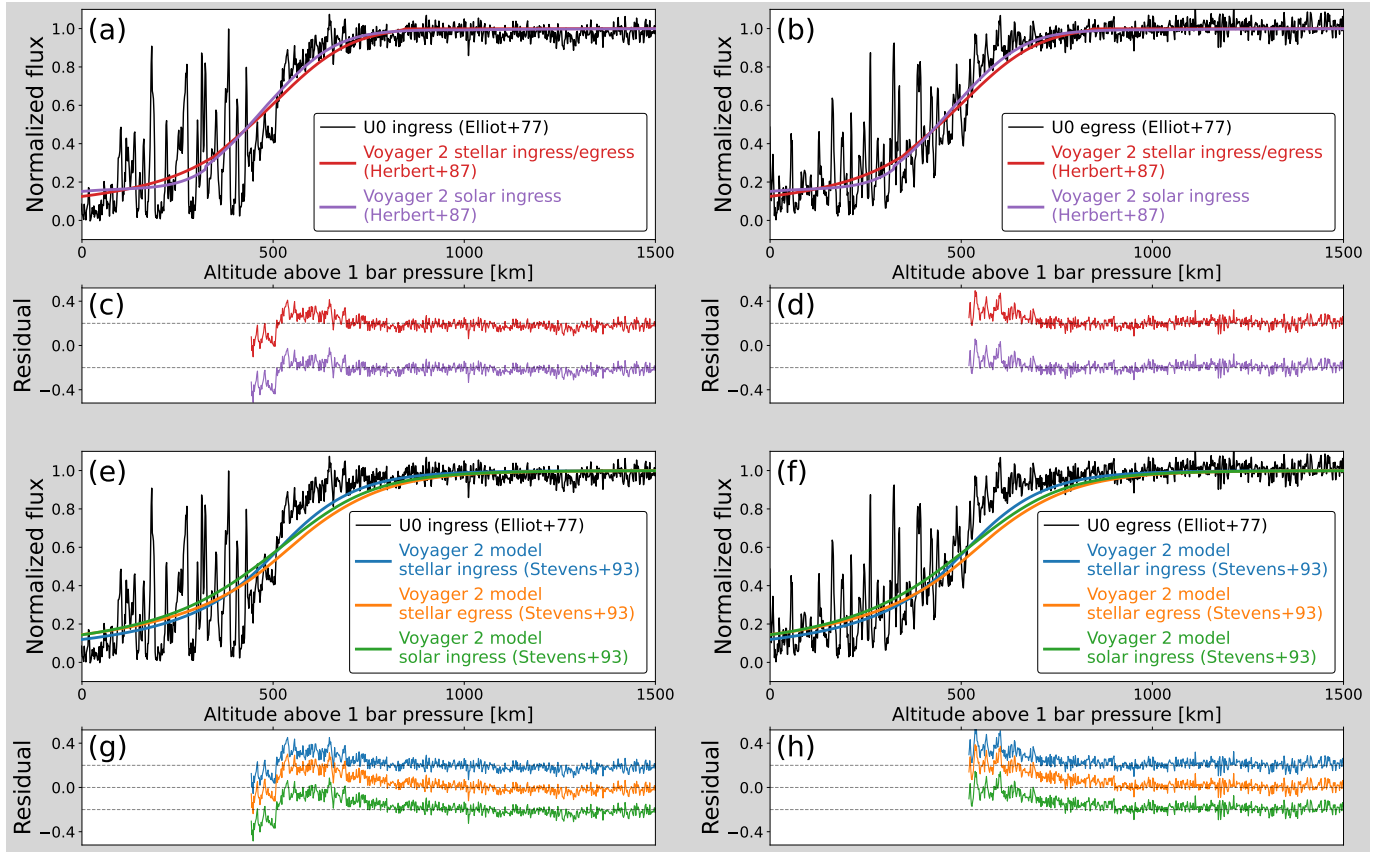
Figure 6. U0 channel 2 ingress light curve (black, left column) and U0 egress light curve (black, right column) compared with simulated H87 profiles (a, b) and S93 simulated profiles (e, f). Subfigures (a), (b), (e), and (f) plot the normalized stellar flux of the light curves versus the projected observer altitude above the 1 bar pressure level. Residuals are shown below each comparison in the same colors (c, d, g, h) and share the abscissa. Notice that all the residuals show scatter near zero above approximately 800 km but diverge significantly from zero at lower altitudes, indicating that the simulated Voyager 2 light curves diverge most strongly from the U0 light curve at the very beginning and end of the occultation.
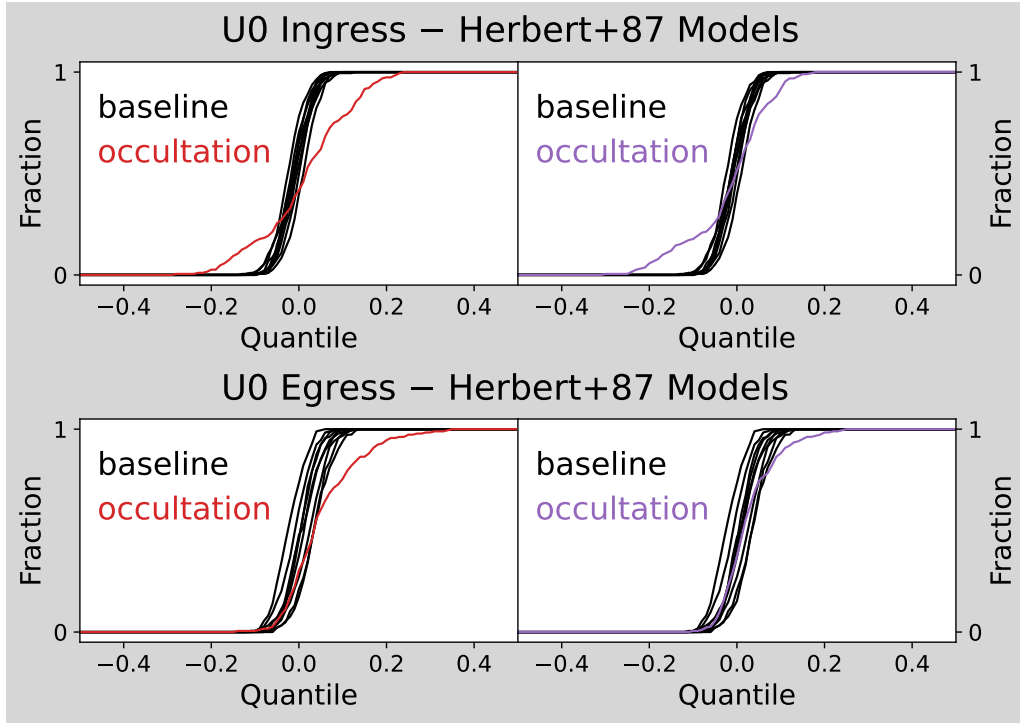
Figure 7. Empirical distribution functions for the H87 Voyager 2 stellar and solar occultation profiles. The residuals shown in Figure 6 were divided into ten blocks, nine of which are baseline (in black) and the other of which is for the occultation (in color). The colors in this figure correspond to the same colors used in Figure 6. Notice that the distribution functions for the occultation blocks are all clearly different from the tightly-grouped baseline distributions, especially at the tails.
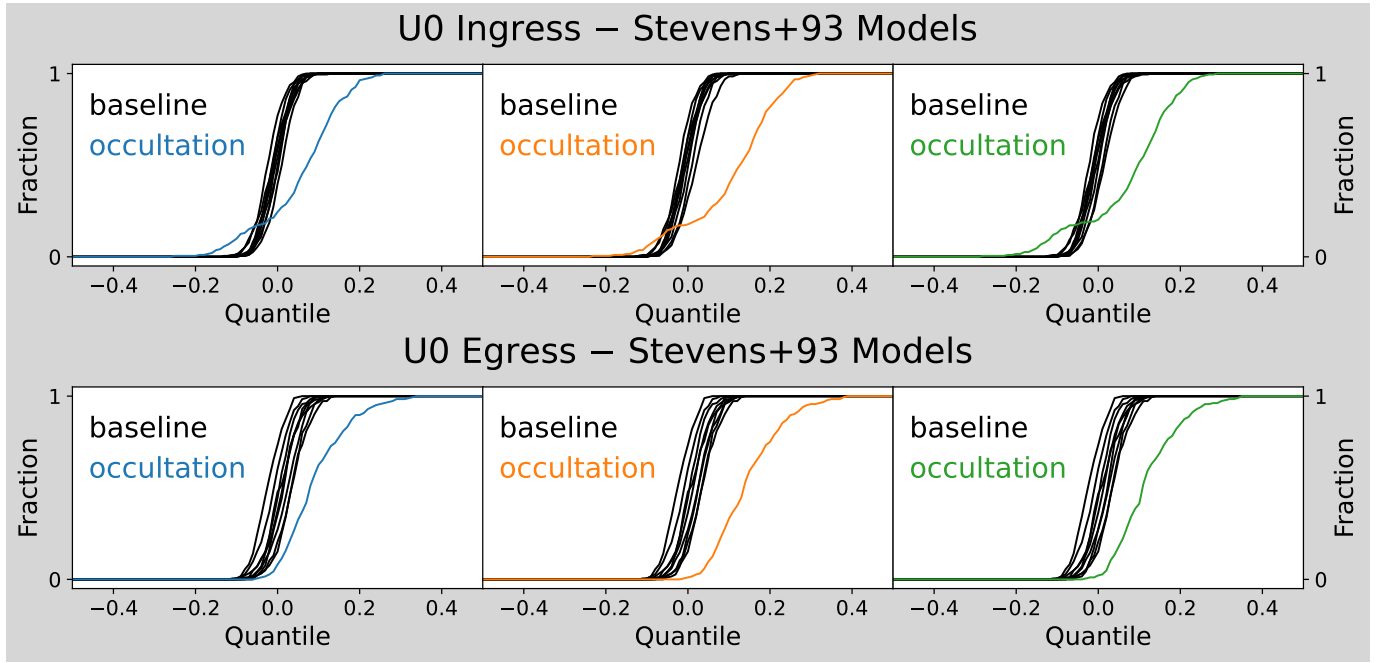
Figure 8. Empirical distribution functions for the S93 Voyager 2 stellar and solar occultation profiles, following Figure 7. The colors in this figure correspond to the same colors used in Figure 6. As in Figure 7, notice that the distribution functions for the occultation blocks are all clearly different from the tightly-grouped baseline distributions, especially at the tails.
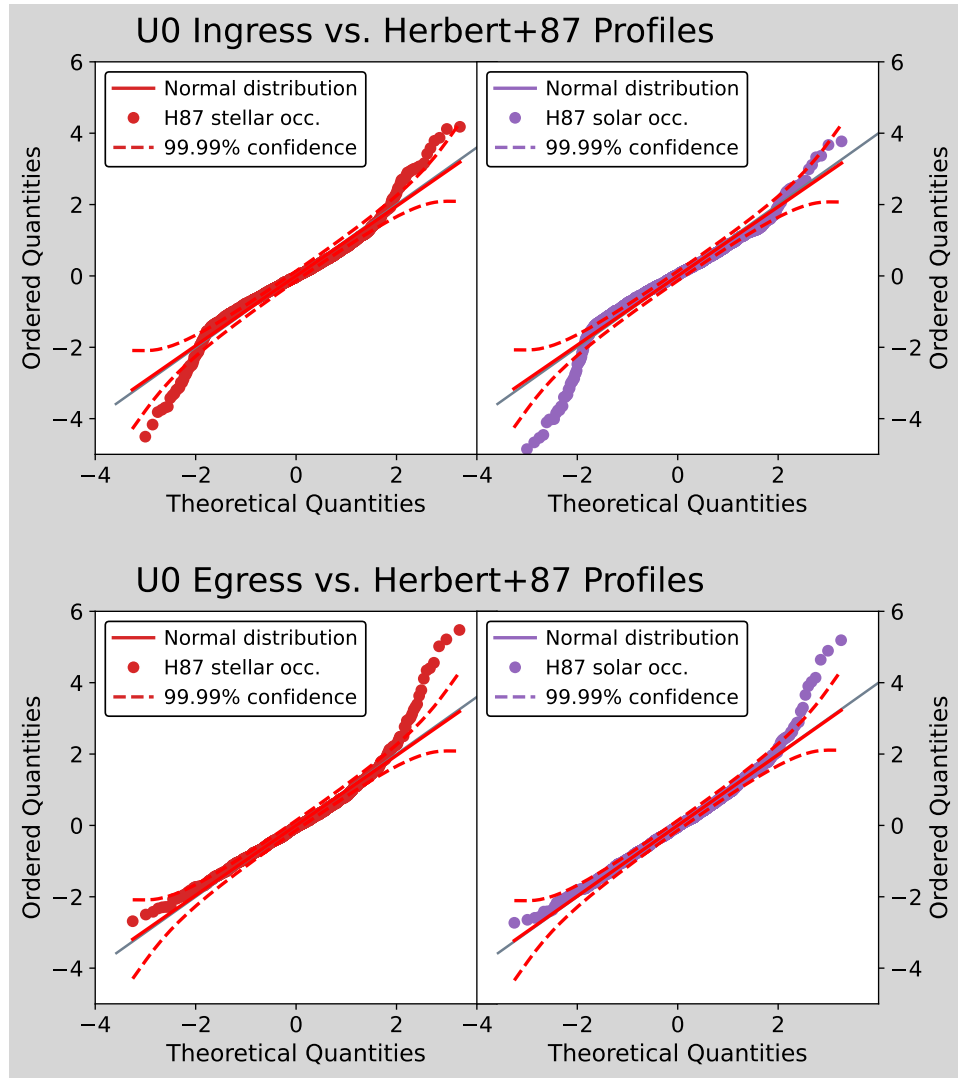
Figure 9. Filled circles show quantile-quantile (Q-Q) values for the H87 residuals shown in Figure 6c–d. Similar to Figures 6c–d, red circles show H87 stellar ingress/egress and purple circles show H87 solar ingress. Quantiles of the residuals are shown on the y-axis versus theoretical quantiles for a normal distribution on the x-axis. The solid red line represents the two distributions being equal and the dashed red lines are the 99.99% confidence intervals. Notice that in all four subplots, the distributions lie outside the confidence intervals in some areas, especially at the tails.
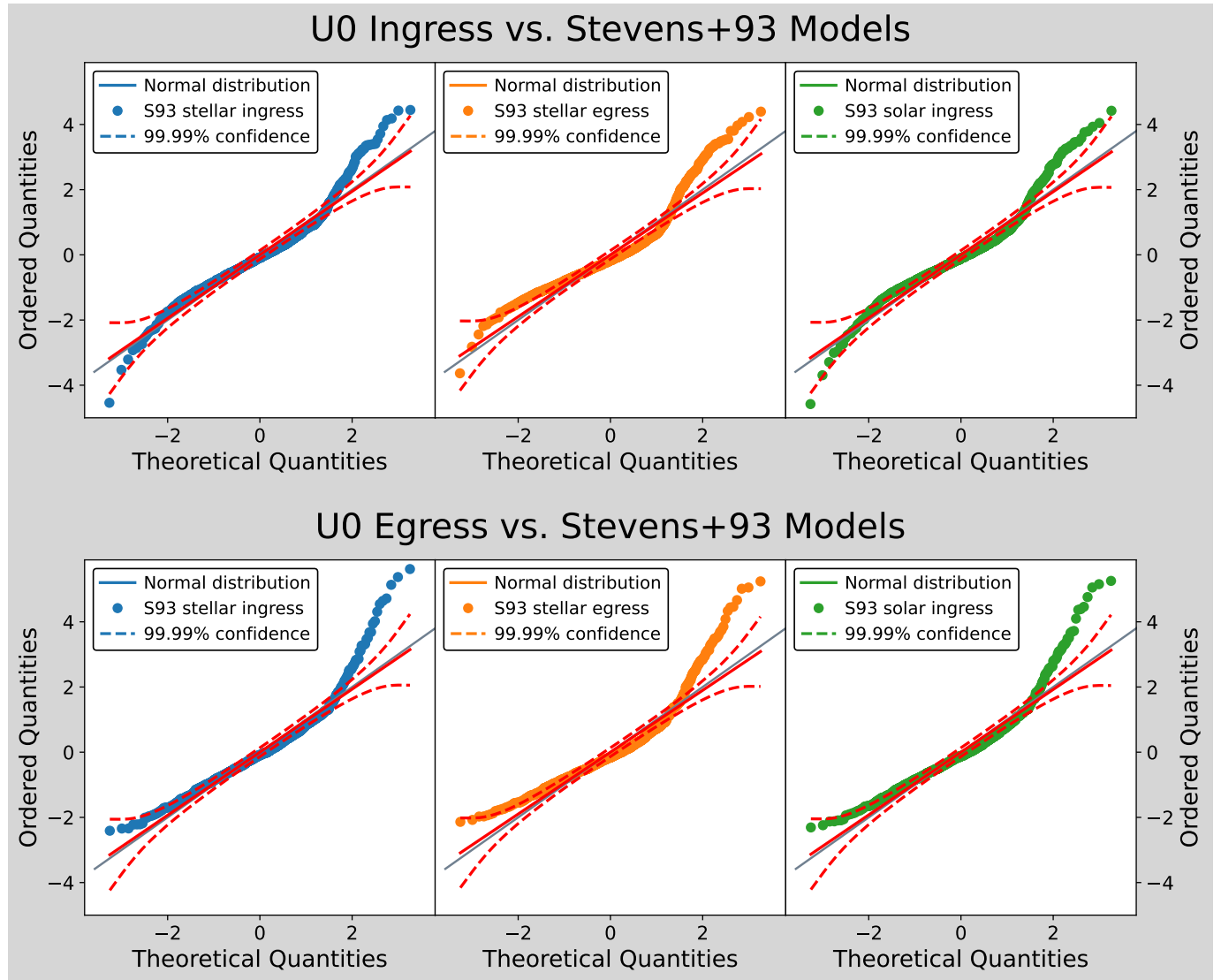
Figure 10. Filled circles show Q-Q values for the S93 residuals shown in Figures 6g–h, as in Figure 9. Similar to Figures 6g–h, blue circles show S93 stellar ingress, orange circles show S93 stellar egress, and green circles show S93 solar ingress. Quantiles of the residuals are shown on the y-axis versus theoretical quantiles for a normal distribution on the x-axis. The solid red line represents the two distributions being equal and the dashed red lines are the 99.99% confidence intervals. Notice that in all six subplots, the distributions lie outside the confidence intervals in some areas, especially at the tails.
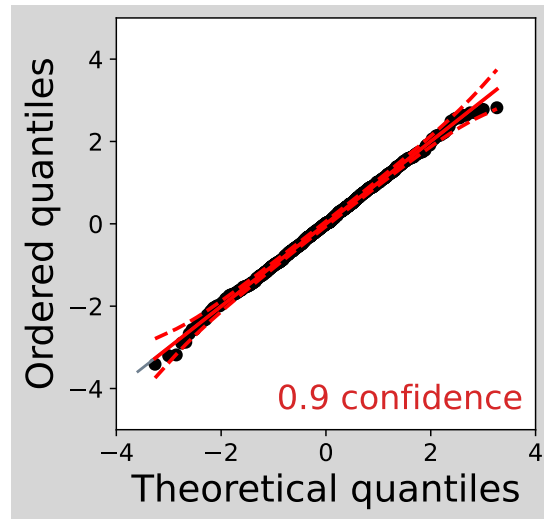
Figure 11. Q-Q plot for a section of baseline residual. Here, the distribution lies entirely within the 90% confidence intervals, meaning we cannot reject the null hypothesis that the baseline of the residuals (away from the occultation) are normally distributed. That is, the baseline distribution fails to clear a low bar (90%) for non-normality, leading to the conclusion that the baseline is normally distributed.
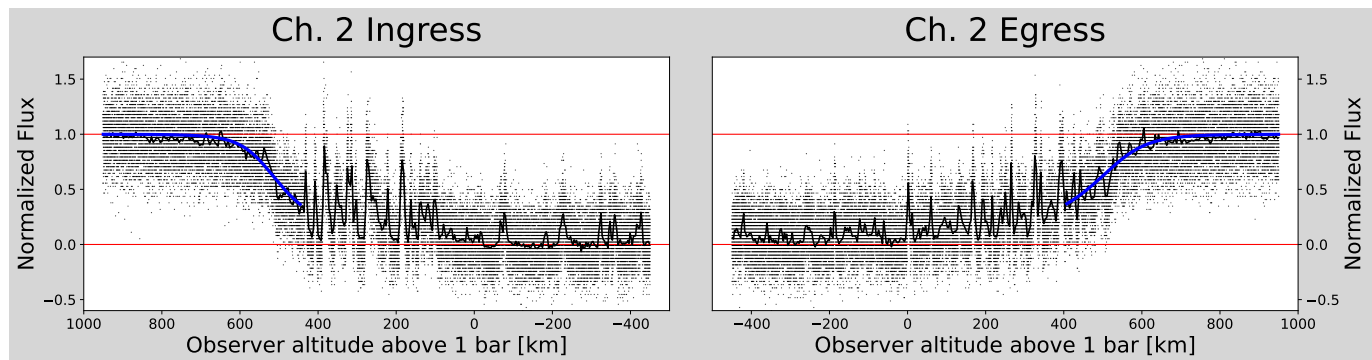
Figure 12. Observer altitude in km versus normalized flux for the channel 2 light curve (ingress and egress), with full resolution in small black points, binned data in black line, and the thermal gradient model fit in blue. We show only channel 2 here because it is the highest signal-to-noise of the three channels.
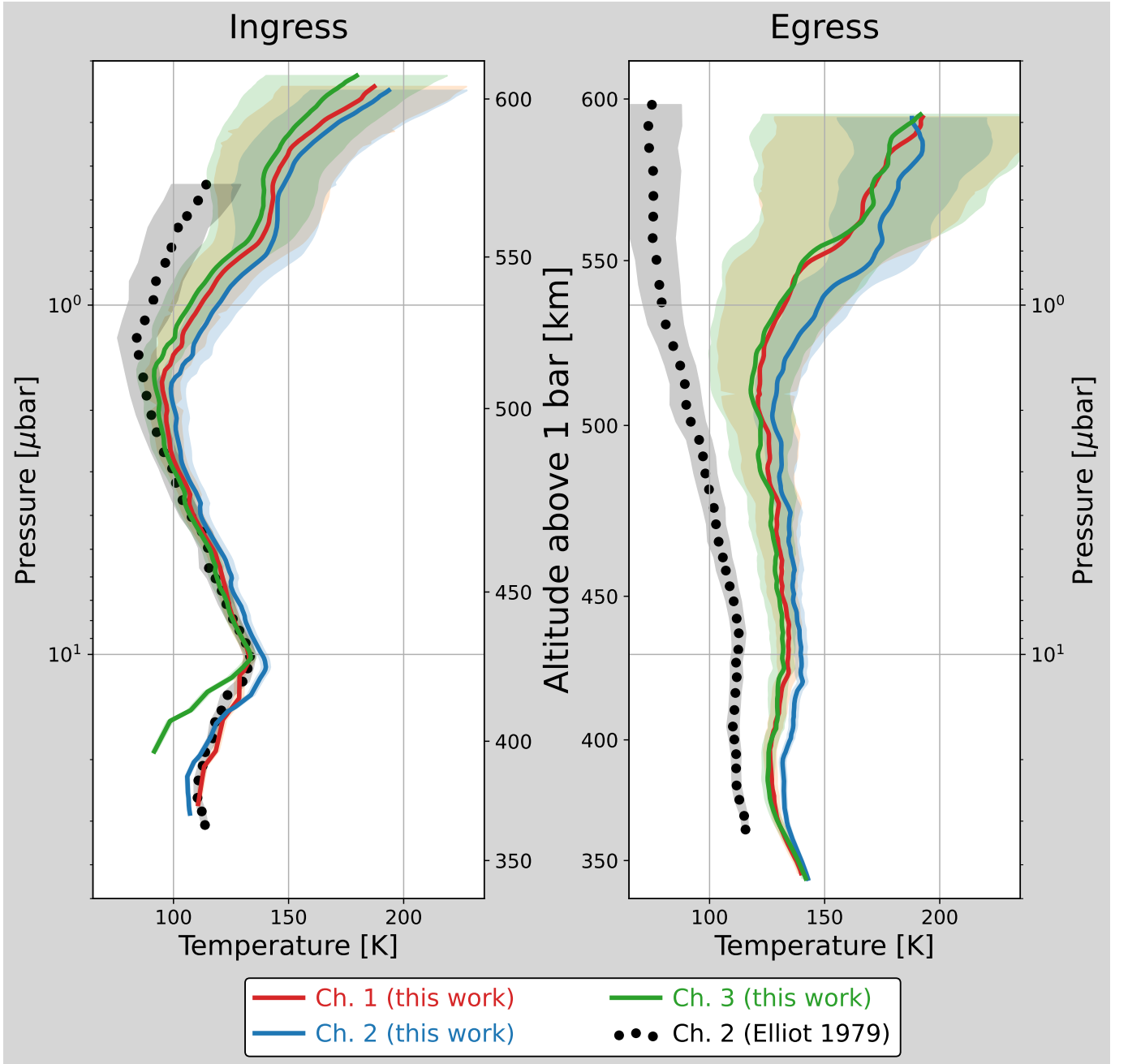
Figure 13. Temperature profiles resulting from reprocessing the U0 light curve, with ingress on the left and egress on the right. The reprocessed results for the three channels are shown with solid lines in red, blue, and green, with 1σ shaded error regions. The originally-published profiles (Elliot & Dunham 1979) are shown in large black dots with 1σ shaded error regions. Temperatures are shown as a function of pressure and the altitudes corresponding to channel 2 of the reprocessed results from this work are shown for reference. Notice that all three reprocessed channels agree with each other (except for the bottom of ingress) and agree with the original profile on ingress, but disagree with the original profile on egress. In addition, the upper ends of all reprocessed profiles show a more rapidly warming lower thermosphere than the original profiles do. The reprocessed profiles have a vertical resolution of sub-1km, increasing slightly to a few km at the bottom of the profiles.
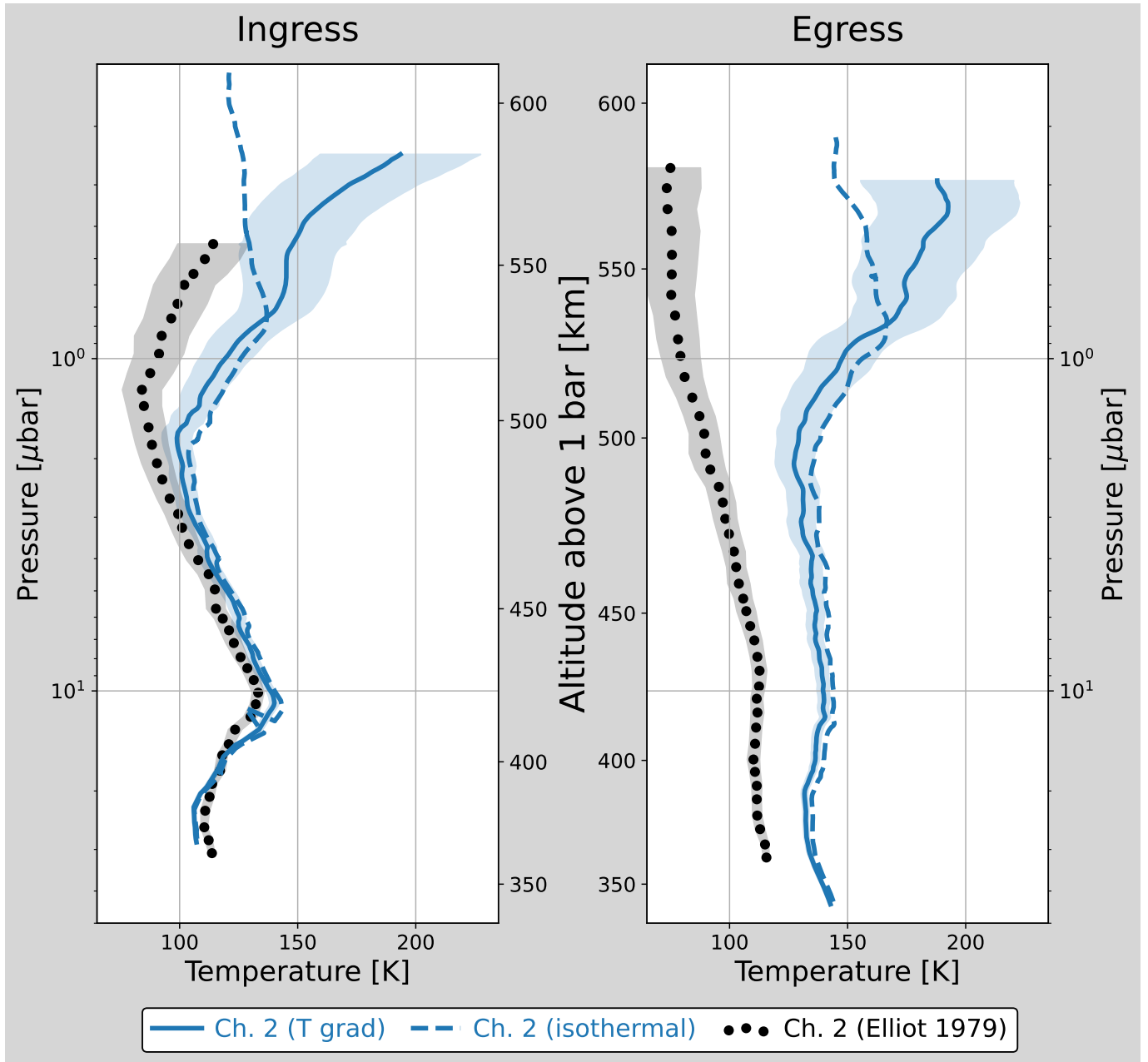
Figure 14. The results of reprocessing the U0 occultation with different boundary conditions. Originally-published profiles (Elliot & Dunham 1979) and reprocessed channel 2 data with a thermal gradient model are shown identically as in Figure 13. The reprocessed channel 2 data with an isothermal model is shown in dashed blue line. The boundary condition strongly impacts only the top end of the profile.
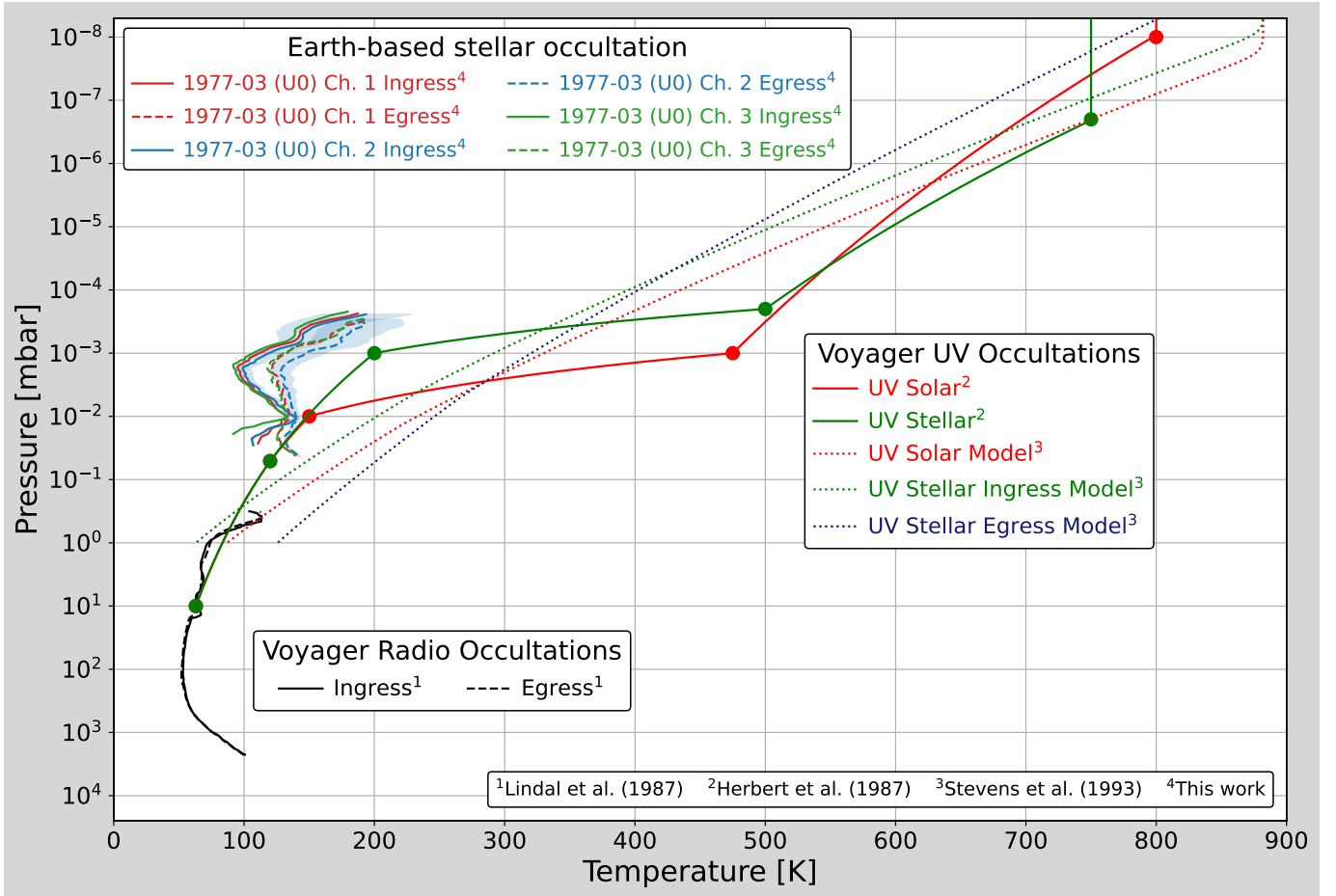
Figure 15. As Figure 1, with the reprocessed U0 results from this work, including shaded 1σ uncertainty regions. Notice that the tension between U0 and Voyager 2 profiles is less prevalent at the 10^{-2} mbar pressure level but still exists at the 10^{-3} mbar pressure level. While the reprocessed profiles may have decreased the tension, stellar occultation processing alone cannot account for it.

Table 1. A list of properties of the observation of U0 aboard the Kuiper Airborne Observatory

Quantity	Value
Primary observer	Jim Elliot, MIT
Observatory	Kuiper Airborne Observatory
Aperture	91 cm
Wavelengths (nm)	Ch. 1: 619, Ch. 2: 728, Ch. 3: 852
Integration	0.01 s
$(S/N)_H$ [a]	Ch. 1: 122, Ch. 2: 178, Ch. 3: 119
Impact parameter	24449 km
Sub-occultation latitude	ingress: $4.5°$N, egress: $18.1°$S

[a] Defined in Equation 1.

Table 2. Table of results from the Anderson-Darling (A-D) test of normality. Each entry in the table is an A-D statistic value. The 99% confidence critical value for each test is given below the table. In all cases, the baseline residuals fail to exceed the critical value while the occultation residuals all exceed the critical value.

	S93 stellar ingress	S93 stellar egress	S93 solar ingress	H87 stellar in/egress	H87 solar ingress
U0 ingress baseline	0.233	0.233	0.233	0.233	0.233
U0 egress baseline	0.391	0.391	0.391	0.391	0.391
U0 ingress occultation	18.169	38.878	24.860	12.651	13.039
U0 egress occultation	15.835	21.421	20.737	8.081	3.546

99% confidence critical value: 1.089

Saunders et al.

Table 3. Parameters for channel 2 model fit. Definitions for each parameter is given below the table. For more details on the model or these parameters, see Elliot & Young (1992).

Parameter	Ingress fit value	Egress fit value
r_H	26078.1 km	26005.4 km
λ_H	881.3 ± 50.1	620.1 ± 25.4
b	158 ± 43	72 ± 24
p_0	0.3 ± 0.11 μbar	0.3 ± 0.09 μbar
T_0	193.0 ± 45.8 K	187.7 ± 33.0 K
n_0	$1.1 \pm 0.14 \times 10^{19}$ m^{-3}	$1.2 \pm 0.16 \times 10^{19}$ m^{-3}
r_0	26147.5 km	26109.1 km

r_H is the half-light radius, the radius at which the model produces a normalized flux of 0.5.

λ is the ratio of gravitational binding energy to the thermal energy of the atmosphere (g/kT). λ_H is the value of λ at the half light radius r_H. It can be thought of as the "puffiness" of the atmiosphere.

b is the exponent in the power law equation for the thermal gradient model (see Section 4).

p_0 is the reference pressure.

T_0 is the reference temperature.

n_0 is the reference number density.

r_0 is the radius at which the other reference quantities apply.